Fluid systems and fracture development during syn-depositional 1 fold growth: an example from the Pico del Aguila anticline, Sierras Exteriores, Southern Pyrenees, Spain.

Nicolas Beaudoin, Damien Huyghe, Nicolas Bellahsen, Olivier Lacombe, Laurent Emmanuel, Frédéric Mouthereau, Laure Ouanhnon

Fluid systems and fracture development during syn-depositional fold growth: an example from the Pico del Aguila anticline, Sierras Exteriores, Southern Pyrenees, Spain.

Nicolas Beaudoin[1,2,3,*], Damien Huyghe[4], Nicolas Bellahsen[1,2], Olivier Lacombe[1,2], Laurent Emmanuel[1,2], Frédéric Mouthereau[1,2], Laure Ouanhnon[1,2].

[1] Sorbonne Universités,UPMC Univ Paris 06, UMR 7193, ISTEP, F-75005, Paris, France.
[2] CNRS, UMR 7193, F-75005, Paris, France.
[3] School of Geographical and Earth Sciences, University of Glasgow, Gregory Building, G128QQ Glasgow, United Kingdom.
[4] UMR 5563 - Geosciences Environnement Toulouse, Université Paul Sabatier Toulouse III, Toulouse, France.

Keywords: Fluid system; Syn-sedimentary fold development; Pyrenean foreland; Fracture population; Sierras Exteriores ; Pico del Aguila anticline.

Abstract

This paper reports an integrated, spatio-temporal analysis of the fracture-controlled paleo-fluid system in the Pico del Aguila anticline, a N-S trending fold located in the Sierras Exteriores, the southern front of the Spanish Pyrenees. Eight fracture sets (joints or faults) are recognized throughout the fold and are separated into a fracture sequence that is defined using field relationships and the remarkable temporal constraints offered by the syn-tectonic sedimentary deposits. This fracture sequence records a complex Paleocene to Early Oligocene structural evolution, including map-view, clockwise rotation and tilting of the fold axis. The geochemical analysis of calcite cements from the different mineralized fracture/vein sets reveals a compartmentalized fluid system during most of fold development. This initial paleofluid system was later perturbed when bending-related fractures associated with foreland flexure and outer arc extension triggered small-scale, vertical fluid migration. Fractures developed in shallow strata facilitated downward migration of surficial fluids that controlled the paleo-fluid system in the Late Priabonian/Stampian continental deposits. The study of the Pico del Aguila anticline depicts for the first time the evolution of a fluid system in a shallow, syn-depositional compressional setting, and results further strengthen the statement that

fluids migrate vertically across stratigraphic boundaries take place during fold hinge-related deformation.

1. Introduction

Fluid-rock interactions during folding control diagenesis and deformation, hydrocarbon migration, and heat transport (Qing and Mountjoy, 1992; Roure et al., 2005; Katz et al., 2006; Lacombe et al., 2014). A recent review of factors governing the temporal and spatial distribution of fluids in folds (Evans and Fischer, 2012) highlights that the development of a sub-seismic fracture network is essential in fluid migration. In particular, the vertical persistence and lateral connectivity of joints usually promotes alternating vertical and lateral fluid migrations at local and large-scale (e.g. Evans and Battles, 1999; Van Geet et al., 2002; Fischer et al., 2009; Barbier et al., 2012a; Beaudoin et al., 2011, 2014). Although no simple rule arises since each natural case of fold-fracture-fluid interactions differs, a common characteristics occurs (Evans and Fischer, 2012): the development of curvature-related fracture sets promotes vertical fluid migration and mixing of various preexisting hydrologic reservoirs delimited by stratigraphic seals. This kind of evolution can be deciphered when both the large faults and the fracture network are studied. Indeed, sub-seismic fracture patterns experience a succession of deformation steps at fold-scale (Stearns and Friedman, 1972; Fischer and Wilkerson, 2000; Bergbauer and Pollard, 2004; Bellahsen et al., 2006a, b; Cooper et al., 2006; Tavani et al., 2006; Beaudoin et al., 2012, 2013). However, most studies were performed in settings where deformation substantially postdates strata compaction (Evans and Battles, 1999; Van Geet et al., 2002; Fischer et al., 2009; Beaudoin et al., 2011, 2014; Barbier et al., 2012a). Consequently, the evolution of fluid-rock interactions in strata folded at shallow depth during sediment deposition remains incompletely documented.

Here, we study the case of the Pico del Aguila anticline, one of the N-S trending folds of the Sierras Exteriores positioned at the southern structural front of the Pyrenees (Fig. 1). The Pico del Aguila anticline is interpreted as a detachment fold with a décollement level located within Triassic evaporitic rocks (Millán, 1996). The growth of the structure is recorded by the syn-tectonic deposition of deep marine to continental sediments from the Late Lutetian to Priabonian times (Millán et al., 1994; Hogan and Burbank, 1996; Castelltort et al., 2003). The kinematics and mechanics of the Sierras

Exteriores and especially the Pico del Aguila anticline have been extensively documented (Millán et al., 1994; Poblet and Hardy, 1995; Poblet et al., 1998; Novoa et al., 2000; Anastasio and Holl, 2001; Castelltort et al., 2003; Nalpas et al., 2003; Huyghe et al., 2009; Vidal-Royo et al., 2012, 2013). Our investigation of the fluid system in the southernmost fold structures of the Pyrenean foreland allows a comparison with recent studies of fluid systems in the northern hinterlandward fault-related folds (Travé et al., 2000, 2007; Lacroix et al., 2011, 2014).

This contribution aims to describe the fracture network in the Pico del Aguila anticline, and then using the remarkable record of fold evolution granted by the growth strata to decipher the history of fracturing. Geochemical analyses of calcite vein cements as well as fault-coating calcite are used to identify and interpret the sources of fluids that flowed in fractures, their pathways, and their interactions with surrounding rocks. Beyond regional implications, results shed light on the evolution of the paleo-fluid system during growth of syn-depositional detachment folds.

2. Geological Setting

The Pico del Aguila anticline is a 160°E trending anticline located in the Sierras Exteriores, a range comprising a set of NW-SE to N-S trending folds markedly oblique to the south-Pyrenean thrust front (Fig. 1). The Sierras Exteriores are located at the southern front of the Jaca piggyback basin, which borders the southwestern part of the Central Pyrenees. The Pico del Aguila anticline plunges 30° toward the North, because it is linked to the late thrusting of the Jaca Basin over the Ebro basin during the activation of the Guarga basement thrust (Fig. 1B, Teixell, 1996; Jolivet et al., 2007). The Pico del Aguila anticline is a detachment fold with a décollement level located within the Triassic evaporite strata (Fig. 2). The growth of this anticline is well-constrained by the wealth of biostratigraphic data (Canudo et al., 1988; Molina et al., 1988; Sztràkos and Castelltort, 2001; Huyghe et al., 2012a) and paleomagnetic studies (Hogan and Burbank, 1996) obtained on Middle Eocene to Oligocene growth strata. The sedimentary succession (Fig. 1C) comprises dolostones and gypsiferous clays composing the Triassic Muschelkalk and Keuper facies, respectively (Millán et al., 1994). The overlying formations are the upper Cretaceous platform limestones of the Adraén-Bona Formation (Fm.), the Paleocene continental and fluvial sandstones and mudstones of the Tremp Fm., and the

Lutetian shallow marine limestones of the Guara Fm. The sedimentary record indicates that folding began during the deposition of the upper part of the Guara Fm. (upper Lutetian, Millán et al., 1994; Huyghe et al., 2012a) and lasted during deposition of the Bartonian-early Priabonian prodeltaic marls of the Arguis Fm. and the Middle-Priabonian marine shallow-deltaic sandstone of the Belsué-Atarès Fm. This interpretation is in accordance with the growth model of Hogan and Burbank (1996) that indicates that folding began during the late Lutetian (42 Ma) and ended during early Priabonian (35 Ma). On top of the latter formation, the Late Priabonian-Stampian continental sandstones and claystones of the Campodarbe Fm. were deposited after folding (Millán et al., 1994). Subsequent thrusting of the Jaca basin over the Ebro basin is due to the development of the southern Pyrenean frontal thrust during Late Oligocene-early Miocene (Millán, 1996; Jolivet et al., 2007; Huyghe et al., 2009).

3. Methodology to decipher fluid-fracture-fold evolution

This work focuses on fracture generations observed in pre-, syn- and post-folding strata of the Pico del Aguila anticline. Fracture generations are mainly composed of joints and veins opened in mode I, as well as faults along which movement is recorded by slickensides. Pressure-solution seams (stylolites) related to both compaction and tectonic loading also occur. Mode I-opening of joints and veins was checked in the field and in thin-sections by the offset of pre-existing elements in the matrix or by the lack of grain crushing in the matrix near the borders of the fractures (Fig. 3a).

Nearly 1500 joint/vein orientation data were collected along with 120 fault-slip data at the outcrop-scale (Fig. 4-7, Table S2 as supplementary material) in different formations (pre-, syn-, and post-folding strata extending from Triassic to Priabonian) and structural positions (hinge and limbs). About 50 sites were defined by a common structural position and bedding dip, half of them being located in the pre-folding strata (25 sites). The post-folding strata of the Campodarbe Fm. have fewer samples in our dataset (6 sites).

3. 1. Identification of fracture sets

Identification of fracture sets is now a well-established and powerful tool to unravel the deformation history of folded strata (eg, Bergbauer and Pollard, 2004;

Bellahsen et al., 2006; Lacombe et al., 2012). Fracture sets can be defined as fracture populations that share a common deformation mode, a common orientation regarding the bedding dip and with statistically consistent chronological relationships compared to other fracture sets. For our study, we compute the mean orientation of measured fractures for each site by means of a Kernel statistical analysis (software developed at IFPEN for the definition of fracture sets, see Bellahsen et al., 2006; Ahmadhadi et al., 2008). This data processing is first done for the present position of strata, then after the correction of the fold axis plunge (by removing the tilt of 30° due to the frontal thrust activity), and in a third step after the removal of the local bedding dip. Results are presented on stereonets for each measurement site at each step (Figs. 3 to 6). Diagrams are not weighted by abundance, as we believe that this modification can be biased by outcrop conditions. However, vertical persistence, spacing or relative abundance of fractures all were considered for the interpretations. Indeed, we believe that a fracture set is relevant to constrain the tectonic evolution of strata only if it is observed everywhere in the fold, or at least in numerous sites from a single structural or stratigraphic position. Therefore, data processing results in the recognition of different fracture sets that are each related to a deformation event. We assume that the development of a fracture set will not overlap the development of another fracture set except if the stress conditions required are similar for these two sets and if chronological relationships suggest synchronism. Consequently, we use chronological relationships to constrain the development of fracture sets through time so to build the fracture sequence.

Four approaches are used to determine the relative age of the different fracture sets: (a) the relative age of fractures based on abutting or offset relationships at field sites; (b) the restriction of fractures to particular units in the pre-, syn- and/or post-folding stratigraphic sequence; (c) the assumption that mode I fractures formed vertically with a horizontal least compressive principal stress (Anderson, 1951); and (d) the assumption that bed-perpendicular fractures striking parallel to the fold axis and located near the hinge of the fold are related to local extension due to strata bending. We carefully observed abutments and crosscutting relationships on pavements at the Pico del Aguila, using a rule that a set composed of fractures that terminate at fractures of another set are inferred to have developed later (Fig. 8). These relationships observed at site-scale are checked on thin sections, and the consistency of the chronology is checked

at the fold-scale. Finally, the sequence is checked with the record provided by growth strata.

3.2. Inversion of fault-slip data for paleostress

Some fracture sets comprise only faults, which slips were inverted to reconstruct the related stress tensor using the inversion methods described in Angelier (1984)(see Lacombe, 2012 for a recent review of fault-slip data inversion for paleostresses). The identification and separation of successive generations of faults and related stress regimes are based on both mechanical incompatibility between individual fault slips (with the computed stress tensor) and relative chronology observations (e.g., superimposed striations on fault surfaces, crosscutting relationships between faults). As with the fracture sets, we provide stereonets to show the results of fault-slip data inversion (1) in the current strata attitude (post-thrusting); (2) after removing the regional tilt of the fold axis due to the activation of the frontal thrust (pre-thrusting and post-folding); (3) and after removing the local bedding dip (pre-folding). If one assumes that a principal stress axis remains generally vertical without local stress rotations, which could be due to stress channelization within shallow-dipping strata separated by low friction interlayers along which bedding-parallel slip occurs (Tavani et al., 2006), (1) inversion of a fault set formed before folding (or thrusting) and measured in a fold limb would have one of the computed stress axes perpendicular to bedding, with the other two lying in the bedding plane; (2) inversion of a post-folding or post-thrusting fault set yields stress tensors with compression horizontal irrespective of bedding dip in the current or pre-thrusting attitude (e.g., Lacombe, 2012). Note that pre-folding stress tensors are presented on Schmidt's stereonets only in cases where stress axes are consistent with these Andersonian conditions once corrected from plunge and/or bedding dip.

3.3. Petrographic and geochemical analyses of veins and host-rock cements

Samples of vein calcite cements and fault-coating calcite within their surrounding matrix were collected in a variety of stratigraphic and structural positions. We use standard and cathodoluminescence petrography, as well as stable isotopes of carbon and oxygen to constrain the geochemistry of the fluids from which calcite precipitated.

Although we observe fluid inclusions in the samples, microthermometric work proved fruitless, and yielded only the observation that the inclusion population was dominated by monophase (liquid), aqueous inclusions (Fig 3 e-f) where the attempts to nucleate vapor bubble by freezing failed. Lack of vapor bubble in inclusions suggests a precipitation of fluids about 80 ± 20°C (Roedder, 1984).

Petrographic and cathodoluminescence observations were conducted on oriented thin-sections of 35 selected samples that are representative of fracture sets observed at the Pico del Aguila anticline. We use observations of vein crystal textures and offset wall-rock markers to constrain the mode of fracture wall displacement (Fig. 3). Microscopy also allowed checking and refining the chronological relationships that have been initially defined from field observations. We use a Cathodyne Opea cold cathode system to examine the cathodoluminescence of the samples (Fig. 9). These observations constrain the number of precipitation events, the conditions of precipitation, and the diagenesis of the veins and host rocks. Operating conditions are in the range of 200–400 lA and 13– 18 kV gun current with a constant 60 mTorr vacuum.

$\delta^{18}O$ and $\delta^{13}C$ have been measured in calcite collected from 70 veins and related host-rocks, covering various structural and stratigraphic positions in the Pico del Aguila anticline (Fig. 10, Table S1). Measurements are performed using an automated preparation device coupled to an Isoprime gas-ratio mass spectrometer. Between 40 and 100 µg of calcite powder is collected from each veins, using either hand-drill or scalpel to avoid mixture with host-rocks. Samples are placed in glass vials and reacted with dehydrated phosphoric acid under vacuum at 90°C, before being measured 10 times each. A correction for dolomite samples was conducted (Rosenbaum and Sheppard, 1986). Hereinafter, all values for both veins and host-rocks are reported in per mil (‰) relative to the Vienna Pee Dee Belemnite (VPDB or PDB) for carbon and for oxygen with an accuracy of 0.05‰ and 0.1‰, respectively (Table S1).

4. Fracture system: observations and interpretations

We present a new geological map, based on recent field observations and high-resolution aerial photographs that slightly differs from the previous maps (Fig. 2; e.g.

Puigdefabregas, 1975; Millán, 1996; Vidal-Royo et al., 2012). The main difference is that Triassic rocks are not observed in the northern part of the fold where sub-vertical limestone strata of the Cretaceous Adraen-Bona Fm. were observed.

Eight fracture sets are defined by field observations, statistical analyses, and stress inversion processes, including 5 joint/vein sets (Figs. 4-6) and 3 striated fault sets (Fig. 7). For the sake of simplicity, the fracture sequence is presented with a nomenclature defined by relative timing with respect to folding (Fig. 8).

Sets J1 and J2 appear mainly in the oldest pre-tectonic formation (Table 1, figs. 4-5-6), making them the oldest fractures to have developed. Both are bed-perpendicular. Once the plunge and local dip are removed, set J1 strikes 120° while set J2 strikes 090°. Cross-cutting relationships show younger J2's abutting against older J1's (Fig. 8-b). Other sets are observed in all stratigraphic units. Set J3 joints and veins strike 070° and are bed-perpendicular, and abut against set J2 fractures (Fig. 8-c). Set J4 joints and veins strike 40° and are bed-perpendicular, reopen J3 fractures and abut against J2 fractures (Fig. 8-c). Sets J3 and J4 are observed in every structural position, whereas set J5 is only observed near the anticline hinge and in the syncline. Set J5 joints and veins are roughly normal to bedding and strike mainly 170°. Chronological relationships from outcrops and thin sections indicate that set J5 is younger than sets J1, J2, J3, and J4 (Fig 8-a,d), whereas chronological relationships with set J4 are ambiguous.

Sets F1, F2 and F3 comprise faults that are defined by a common causative paleostress reconstructed using a stress inversion process (Fig. 7). Because the lack of crosscutting relationships, the chronology of these fault sets is poorly constrained by field and petrographic observations. Age of the fault sets with respect to folding and thrusting events can however be assessed by assuming that they developed when the stress tensor has a vertical principal stress, as predicted by Anderson (1951). Set F1 comprises steeply dipping, N-S striking normal faults that were only observed at the fold hinge, and developed under an E-W extensional stress regime during folding (Fig. 7). Set F2 comprises newly-formed N-S reverse faults (ex: site 434, Fig. 7) with strike-slip reactivation of fractures oriented 045°E/060°E (ex: site 433-2, Fig. 7) and 160° (ex: 474, Fig. 7), and are compatible with a nearly E-W compression which respect to Anderson's theory in the current attitude of strata or just plunge-corrected, meaning they developed since post-folding. Lastly, set F3 comprise a group of conjugate E-W reverse faults that formed in a predominantly N-S compressional stress regime (ex: site 136-1, Fig. 7).

These faults developed after folding, some of them postdate thrust activation (ex: site 136-1, Fig. 7) while the observed orientation, motion and steep angle of some other reverse faults (ex: site 34, Fig. 7) suggests that they developed at a lower angle during the thrusting.

Prior work has shown that the area of the southern Pyrenean thrust front experienced rotation around a vertical axis. This rotation is interpreted as being related to the southwestward propagation of the deformation in the south Pyrenees and is believed to partially explain the N-S striking of the folds in the Sierras Exteriores. Rotations of 15° to 50° have been proposed from paleomagnetic studies (Pueyo et al., 2002; Oliva-Urcia and Pueyo 2007) and on displacement field reconstruction (Huyghe et al., 2009). Timing of such a rotation for the Pico del Aguila area is inferred to have started as soon as Bartonian and terminated during Oligocene times (Huyghe et al., 2009).

Consequently, this rotation history is of primary importance for interpreting the fracture sequence with respect to anticline development (Fig.11). Drawing on timing of sedimentation with respect to folding (Fig. 1B), and on the stratigraphic distribution of the fracture sets (Figs. 3 to 8, Table 1), we propose that the progressive development of fractures from a 090° strike (set J2 only in oldest strata) to a 040° strike (set J4 in all strata) reflects a progressive clockwise rotation (Fig. 11). Joint sets J2 to J4 are inferred to have formed sequentially parallel to the direction of maximum contraction as part of the structural suite recording regional layer-parallel shortening (LPS) that we here documented as striking NE-SW (Fig. 11-a-b-c (2)). This interpretation is based on (1) the established existence of a rotation in the area, (2) the fact that set J2 is a bed-perpendicular, fold-axis perpendicular-striking set of joints which can be related to LPS (e.g. Bellahsen et al., 2006a), and (3) the stratigraphic distribution of fracture sets, where J2 is observed only in prefolding and prerotation Guara Fm. (Huyghe et al., 2009) while J3 and J4 developed also in syn-rotation strata (Table 1). The angular difference in present-day strikes for sets J2 to J4 is 50°, which we infer to reflect the maximum magnitude of the rotation around a vertical axis (Fig.11-a-b-c). Our interpretation differs from previous work that predicts a rotation of only 20° at the Pico del Aguila (Huyghe et al., 2009). Considering our data, because of possible local heterogeneities and bed-scale stress perturbations, the strikes of fracture sets are only given within 10° of accuracy

(Table 1). Given this limitation and considering mean strikes for each fracture set, the minimal value for the vertical rotation is the difference between J2's (80°) and J4's (50°) strikes. Therefore, our dataset suggests a vertical rotation of about 30° and is more likely considering results from other studies (Pueyo et al., 2002; Oliva-Urcia and Pueyo 2007, Huyghe et al., 2009).

We infer that set J1 predates the rotation and its final orientation fully records the rotation. Given a present day strike of 120°, the regional trend of J1 before the rotation would be 090° (Fig. 11-a (1)). Thus, the joints could be interpreted as having developed during N-S extension related to foreland flexure and/or forebulge in the area (Hervouët et al., 2005). Set J5 is inferred to have developed at the anticline hinge during outer-arc bending that occurred during vertical axis rotation. As these fractures reflect hinge-related deformation, their orientation remained parallel with the anticlinal hinge as it rotated (Fig. 11 a-b-c). Similarly, during fold growth, hinge extensional strain was accommodated by development of F1 faults that were also rotated with the anticline as it grew and spun (Fig. 11-c (3)). Crosscutting relationships between J4 and J5 are ambiguous, so the development of J4 fractures parallel to regional contraction could have been before or coeval with local extension at the hinge.

After rotation around a vertical axis was completed (Fig. 11-d (4)), fold tightening locally perturbed tectonic stress that became perpendicular to fold axis (e.g., Amrouch et al., 2010), in response to which set F2 formed. Later, the Pyrenean-related N-S contraction triggered E-W-trending thrusts ramps (Teixell, 1996; Jolivet et al., 2007), tilted the folds axis during its overthrusting above the 30°-dipping frontal ramp and caused E-W small reverse F3 faults (Fig. 11-d (5)).

The proposed fracture sequence reflects a tectonic history starting from foreland flexure and/or forebulge until the late activation of regional thrusts due to Pyrenean N-S orogenic contraction. Similar relationships between regional-scale foreland flexure and the development of systematic sets of parallel joints/veins have been proposed in other foreland basins (Billi and Salvini, 2003; Beaudoin et al., 2012; Quintà and Tavani, 2012), and supports a growing body of evidence that many fractures observed in folded strata may in fact predate folding history (e.g., Bergbauer and Pollard, 2004; Bellahsen et al., 2006a; Ahmadhadi et al., 2008; Lacombe et al., 2011; Quinta and Tavani, 2012).

5. Fluid system: observations and interpretations

334

335 *5.1. Sample selection according to microstructural observations*

336 Using observations of veins and surrounding host-rocks from optical and
337 cathodoluminescence microscopy (Fig. 3, 9), four different textures in veins can be
338 described, following the classifications of Durney and Ramsay (1973) and Machel
339 (2000).

340 The textures are (1) blocky calcite with single-phase, bright orange luminescence with
341 brighter fringes at the external rim of crystals (Fig. 9-a); (2) blocky calcite with grain-
342 scale luminescence zonation from bright to dull orange luminescence (Fig. 9-b); (3)
343 Elongated blocky veins with orange luminescence variation in the vein while each
344 fibrous crystal has homogeneous luminescence (Fig. 9-c); and (4) Crack-seal textures
345 characterized by fringes of fine stretched grains on the outer bound of the vein
346 recording one single (Fig. 3-d) or multiple (Fig. 3-a) events. The four textures are
347 observed in all veins sets, so correlation does not exist between texture and either with
348 stratigraphic position or structure or vein set, suggesting precipitation mechanisms
349 independent from these parameters.

350 Textures in veins can be used as indicators of mode I opening and for a single
351 event of fluid precipitation. Blocky calcite texture showing growth competition (Fig. 3-d)
352 is symptomatic of a single fluid precipitation event (Bons et al., 2012). Most of veins
353 from our samples displays such a texture, and cathodoluminescence observed in case
354 (1) (Fig. 9-a) is related to dynamic recrystallization due to growth competition (Machel,
355 2000), while small-scale zonation of case (2) reflects slower precipitation under variable
356 redox condition or simply variation in precipitation kinetics (Machel, 2000). Elongated
357 blocky veins described as texture (3) (Figs. 3-b, 9-c) can be interpreted to reflect
358 precipitation kinetics of fluid equivalent to opening kinematics of the fracture (Bons et
359 al., 2000). Also, the elongation direction relates to the direction of opening of veins, and
360 is useful to distinguish mode I veins fractures (Fig. 3-b) from oblique opening veins
361 fractures (Fig. 3-a), where the latter were discarded from our geochemical study. Finally,
362 multiple crack-seal events were discarded for geochemistry (Fig. 3-a) as they reflect
363 multiple or discontinuous fluid precipitation events, possibly involving different sources
364 (Bons et al. 2000).

365

366 *5.2. Fluid sources from isotopic measurements*

To interpret the geochemical dataset in terms of fluid system evolution, we divided the data into pre-, syn-, and post-folding groups based on host stratigraphic units to determine if isotopic data from veins and host rock show correlations with stratigraphy and/or fold timing (Fig. 10, Table 2). Considering the data this way, we identify four patterns: (1) Veins from Triassic Fms. and some veins from pre-folding Guara Fm. exhibit $\delta^{18}O$ and $\delta^{13}C$ values lower than those of their host-rocks; (2) all other veins belonging to pre-folding formations exhibit $\delta^{18}O$ values lower than those of their host-rocks, while simultaneously exhibiting $\delta^{13}C$ values that are broadly similar to those of their host-rocks. (3) Veins in the syn-folding Arguis Fm. have $\delta^{18}O$ and $\delta^{13}C$ similar to their host-rock values. (4) Veins from the post-folding Campodarbe Fm. exhibit $\delta^{18}O$ values that are significantly greater than their host-rock values, but $\delta^{13}C$ values similar to their host-rock values. These four patterns in the data suggest that fluids from different sources interacted with the host-rocks before, during and after folding, such that fluid flow and precipitation were a function of stratigraphic interval and deformation timing.

Isotopic disequilibrium in vein cements that belong to pattern (1) suggests an opening of each reservoir to an external source of fluids, characterized by negative $\delta^{13}C$ values. As shown in Fig. 10-a, the low $\delta^{13}C$ values in some Guara Fm. and Triassic veins seem to match those of host rocks in the Paleocene Tremp Fm, and we note that the negative $\delta^{13}C$ values are consistent with sedimentary rocks inferred to represent paleosoils and lakes (Pujalte et al., 2009) that contain organic matter. The shallow burial depth attained in this area makes it unlikely that the lower $\delta^{13}C$ values in veins reflect the influence of hydrocarbons. Instead, we infer paleohydrological connection and mixing between fluids from these Paleocene and Triassic units. Interestingly, this connection is recorded broadly in veins of sets J1 and J5, meaning that most of the vertical fluid migration between units was triggered by curvature-related fractures, either due to folding or to regional foreland flexure (Fig. 12-a).

Isotopic patterns of cases (2) and (3) reflect a closed stratified fluid system that experienced a different evolution regarding the timing of deposit of host-rock regarding evolution of folding (Fig. 10-a,-b):

- Veins in pre-folding formations that are not case (1) can be defined by isotopic pattern (2). The lower $\delta^{18}O$ of veins relative to host rocks can be interpreted resulting from precipitation of local fluids after a burial (e.g. Ferket et al., 2000; Travé et al., 2007; Fitz-

Diaz et al., 2011; Evans et al., 2012; Vandeginste et al., 2012). According to the isotopic difference between veins and host-rocks (Δ on Fig. 10-b) and considering temperature-dependent fractionation between H_2O and $CaCO_3$ after Kim and O'Neil (1997), we estimate that pore fluids precipitated 30°C higher than host-rock precipitation temperature. Considering "normal" geothermal gradient, this interpretation implies a burial of 1km, consistent with the sedimentary history (Vidal-Royo et al., 2012).

- Syn-folding formation is characterized by an isotopic equilibrium between veins and host-rocks (case (3)) that reflects local pore-fluids precipitation without significant change in temperature since host-rock underwent diagenesis. This is consistent with the limited burial experienced by the Arguis Fm. after it deposited in the area of the Pico del Aguila (Millán, 1996).

The isotopic pattern of case (4) in the post-folding Campodarbe Formation is inferred to represent an opening to external source of fluids characterized by a higher $\delta^{18}O$ values. According to the continental paleo-environmental conditions at that time (Millán, 1996), such a source could be either river-derived fluid or meteoric fluids. As river-derived fluids isotopic range cannot be used to explain the measured signatures (-8‰ to -5.5‰PDB, Zamarreno et al., 1997, Huyghe et al., 2012b), we propose that isotopic signatures of case (4) record precipitation from meteoric fluids.

6. Discussion : fluid-rock evolution during syn-depositional folding

In their recent review focusing on fold-related fluid systems, Evans and Fischer (2012) stressed the fact that these fluid systems have some common characteristics before and during folding. Analysis of paleo-fluid systems during growth of both detachment and basement-cored folds show that fluid systems are compartmentalized by stratigraphy and exhibit little vertical fluid migration. During subsequent folding, syn-folding joints and faults rupture stratigraphic seals and trigger vertical fluid migration and mixing.

The fluid system evolution of the Pico del Aguila (Fig. 12-a) is accordingly interpreted as a stratified fluid system during most of the geological history, with a strong control of lithology on the fluid isotopic signatures (e.g. Fischer et al., 2009; Evans and Fischer, 2012). However, inter-formational fluid flow is documented for sets J1 and J5, which are related to flexural forebulge and local extension due to folding,

433 respectively. Once the paleo-environment switches from marine to continental during
434 Priabonian (Millán, 1996), the source for formational fluid switched from marine-
435 derived pore fluids to surficial, likely meteoric-derived fluids.

436 The likely common opening of fluid systems to vertical migration during folding
437 (e.g., Evans and Fischer, 2012, Fig.12) is therefore once more supported by the Pico del
438 Aguila case study. Opening during flexural forebulge has also been documented in the
439 Bighorn Basin (Beaudoin et al., 2014). Being the first syn-depositional fold developed at
440 shallow depth for which the fluid system has been studied, the Pico del Aguila
441 additionally illustrates, beyond the strong lithological control on the fluid system, the
442 progressive switch from marine to continental environment as documented by $\delta^{18}O$
443 values of calcite-cemented veins. This interpretation is consistent with observations of
444 current fluid flow in anticlines developed at shallow or significant water depth as in the
445 Central Basin in Iran or in Brunei (Morley et al., 2014). The difference in burial depth at
446 the time of deformation also impacts on the scale of the vertical migration triggered by
447 effective tension-related fracture sets (Fig. 12). For example in a deep buried basement-
448 cored fold, such as the Sheep Mountain anticline (Fig. 12-a, Beaudoin et al., 2011),
449 curvature-related fractures developed enough vertical permeability to allow fluid from
450 depth to invade all the strata, while such big-scale migration is not recorded for the Pico
451 del Aguila (Fig. 12-b). This difference could be directly related to the limited burial and
452 related mechanical compaction of the reservoir, and could illustrate the influence of
453 mechanical properties of strata on hydraulic behavior of curvature related fractures, as
454 highlighted in numerous natural cases (Cooke, 1997; Fischer and Jackson, 1999;
455 Laubach et al, 2009; Savage et al., 2010; Barbier et al., 2012a; b; Morley et al., 2014).

456 More generally, studies of regional fluid flows in the southern Pyrenean foreland
457 depict large-scale flows of hydrothermal fluids in structures closer to the Pyrenean
458 range (Travé et al., 2000; 2007), and in the Gavarnie thrust, structurally above the
459 Guarga thrust (McCaig et al. 1995; Henderson and McCaig, 1996; McCaig et al., 2000). In
460 the Pico del Aguila, no hydrothermal fluid flow overprinted the system during activation
461 of the underlying Guarga thrust that developed set F3 faults, in which syn-kinematic
462 calcite coating precipitated from local fluids (Table S1). The lack of evidence of deep
463 fluid flow has also been documented along the thrust system of the Monte Perdido,
464 South of Gavarnie (Lacroix et al., 2011) and can be related to the large distance from the
465 range (Figure 1, Lacroix et al., 2014). Alternatively, this lack could be related to limited

faults and joints development after folding. The related vertical permeability creation was too limited and prevented fluids from the basement to flow through the non-permeable evaporites underlying the limestone. Such a case is opposed to what can happen in a basement-cored fold (Fig. 12-a).

7. Conclusions

1. The sub-seismic fracture pattern recognized in folded strata of the Pico del Aguila anticline comprises 8 sets of joints/veins and faults. The oldest fracture set is likely related to the regional-scale foreland flexure that affected strata during Lutetian and therefore clearly predates folding history. Three fracture sets (J2 to J4) then developed in progressively youngering strata, recording a clockwise vertical-axis rotation of the area. Their E-W to NE-SW trends indicate that they developed under a far-field, relatively static NE-SW shortening during the 30-40° rotation around a vertical axis. Among the four remaining sets, two are related to local outer-arc extension during folding (sets J5 and F1), one is related to E-W compression during late-stage fold tightening (set F2), and the last is a set of post-thrusting faults (set F3) that formed in the same N-S compressional stress regime that activated the Guarga basement thrust.

2. The paleo-fluid system related to the fracture pattern is stratified and controlled by depositional environments during most of the history of vein mineral precipitation. The development of regional-scale foreland flexure and local-scale strata curvature-related vein sets triggered small-scale, interformational, vertical fluid migrations between Triassic and Paleocene reservoirs. The progressive switch from marine to continental paleo-environment occurring during Priabonian is recorded by a change of fluid source from local marine fluids to terrestrial surficial fluids.

3. Our interpretation of the fluid system in the Pico del Aguila anticline supports the hypothesis that fluid systems exhibit a common behavior during folding, wherein curvature-related joints facilitate vertical migration of fluids from one hydrostratigraphic reservoir to another. It also illustrates that the extent of such a vertical migration may be strongly reduced when folding affects poorly compacted sediments. Other similar case studies are needed to confirm if the fluid system evolution deciphered in the Pico del Aguila anticline is archetypal of fold-related fluid systems in shallow, syn-tectonic sedimentary settings.

Acknowledgments

Authors thank N. Labourdette for analytical support and F. Delbas for thin-sections. Authors are grateful to M. Fischer, M. Evans, and Editor W. Dunne for their inspiring and highly helpful reviews, which have significantly improved this manuscript. S. Castelltort is thanked for help in the field and fruitful discussions. This work was supported by ISTeP and material support of LFC-R laboratory.

References

Ahmadhadi, F., Daniel, J.M., Azzizadeh, M., Lacombe O., 2008. Evidence for pre-folding vein development in the Oligo-Miocene Asmari Formation in the Central Zagros Fold Belt, Iran. Tectonics 27, TC1016, doi:10.1029/2006TC001978

Anderson, E. M., 1951. The Dynamics of Faulting and Dyke Formation with Application to Britain. Oliver & Boyd, Edinburgh.

Angelier, J., 1984, Tectonic analysis of fault slip data sets. Journal of Geophysical Research 89, 5835–5848.

Amrouch, K., Lacombe, O., Bellahsen, N., Daniel, J.-M., Callot, J.-P., 2010. Stress and strain patterns, kinematics and deformation mechanisms in a basement-cored anticline: Sheep Mountain Anticline, Wyoming. Tectonics 29, TC1005, 1–27, doi:10.1029/2009TC002525 .

Anastasio, D.J., Holl, J.E., 2001. Transverse fold evolution in the External Sierra, southern Pyrenees, Spain. J. Struct. Geol. 23, 379–392.

Barbier, M., Leprêtre, R., Callot, J.-P., Gasparrini, M., Daniel, J.-M., Hamon, Y., Lacombe, O., Floquet, M., 2012a. Impact of fracture stratigraphy on the paleo-hydrogeology of the Madison Limestone in two basement-involved folds in the Bighorn basin, (Wyoming, USA). Tectonophysics, thematic issue : « Into the deformation history of folded rocks » , O. Lacombe, S. Tavani, R. Soto (eds), 576–577, 116-132.

Barbier, M., Hamon, Y., Callot, J.-P., Floquet, M., Daniel, J.-M., 2012b. Sedimentary and diagenetic controls on the multiscale fracturing pattern of a carbonate reservoir: The Madison Formation (Sheep Mountain, Wyoming, USA). Mar. Pet. Geol. 29, 50–67.

Beaudoin, N., Bellahsen, N., Lacombe, O., and Emmanuel, L., 2011. Fracture-controlled paleohydrogeology in a basement-cored, fault-related fold: Sheep Mountain Anticline, Wyoming, United States. Geochemistry Geophysics Geosystems 12, Q06011, doi: 10.1029/2010GC003494.

Beaudoin, N., Bellahsen, N., Lacombe, O., Emmanuel, L., Pironon, J., 2014. Crustal-scale fluid flow during the tectonic evolution of the Bighorn Basin (Wyoming, USA). Basin Research 26, 403-435.

Beaudoin, N., Lacombe, O., Bellahsen, N., Emmanuel, L., 2013. Contribution of Studies of Sub-Seismic Fracture Populations to Paleo-Hydrological Reconstructions (Bighorn Basin, USA). Procedia Earth Planet. Sci. 7, 57–60.

Beaudoin, N., Leprêtre, R., Bellahsen, N., Lacombe, O., Amrouch, K., Callot, J.-P., Emmanuel, L., Daniel, J.-M., 2012. Structural and microstructural evolution of the Rattlesnake Mountain Anticline (Wyoming, USA): new insights into the Sevier and Laramide orogenic stress build-ups in the BigHorn Basin. Tectonophysics, thematic issue : « Into the deformation history of folded rocks » , O. Lacombe, S. Tavani, R. Soto (eds), 576–577, 20-45.

Bellahsen, N, Fiore, P., Pollard, D., 2006a. The role of fractures in the structural interpretation of Sheep Mountain Anticline, Wyoming. J. Struct. Geol. 28, 850–867.

Bellahsen, N., Fiore, P., Pollard, D., 2006b. From spatial variation of fracture patterns to fold kinematics: A geomechanical approach. Geophysical Research Letters 33, L02301, doi:10.1029/2005GL024189.

Bergbauer, S., 2007. Testing the predictive capability of curvature analyses. Geol. Soc. London, Spec. Publ. 292, 185–202.

547 Bergbauer, S., Pollard, D.D., 2004. A new conceptual fold-fracture model including prefolding joints, based
548 on the Emigrant Gap anticline, Wyoming. Geol. Soc. Am. Bull. 116, 294 – 307.

549 Billi, A., Salvini, F., 2003. Development of systematic joints in response to flexure-related fibre stress in
550 flexed foreland plates: the Apulian forebulge case history, Italy. J. Geodyn. 36, 523–536.

551 Bodnar, R., 1993. Revised equation and table for determining the freezing point depression of H2O-Nacl
552 solutions. Geochimica et Cosmochimica Acta 57, 683–684.

553 Boles, J. R., Eichhubl, P., Garven, G., Chen, J, 2004. Evolution of a hydrocarbon migration pathway along
554 basin-bounding faults: Evidence from fault cement. AAPG Bull. 88, 947–970.

555 Bons, P., Elburg, M. A>, Gomez-Rivas, E., 2012. A review of the formation of tectonic veins and their
556 microstructures. Journal of Structural Geology 43, 33-62.

557 Canudo, J.-I., Molina, E., Riveline, J., Serra-Kiel, J., Sucunza, M., 1988. Les évènements biostratigraphiques
558 de la zone prépyrénéenne d'Aragon (Espagne), de l'Eocène Moyen à l'Oligocène Inférieur. Revue de
559 Micropaléontologie 31, 15-29.

560 Castelltort, S., Guillocheau, F., Robin, C., Rouby, D., Nalpas, T., Lafont, F., Eschard, R., 2003. Fold control on
561 the stratigraphic record: a quantified sequence stratigraphic study of the Pico del Aguila anticline in
562 the south-western Pyrenees (Spain). Basin Research 15, 527-551.

563 Cooke, M., 1997. Predicting fracture localization in folded strata from mechanical stratigraphy and fold
564 shape: Case study of east Kaibab Monocline, Utah. Int. J. Rock Mech. Min. Sci. 34, 56.

565 Cooper, S.P., Goodwin, L.B., Lorenz, J.C., 2006. Fracture and fault patterns associated with basement-cored
566 anticlines: The example of Teapot Dome, Wyoming. Am. Assoc. Pet. Geol. Bull. 90, 1903–1920.

567 Durney, D.W., Ramsay, J.G., 1973. Incremental stramsmeasured by syntectomc crystal growths In Gravtty
568 and Tectomcs (edited by De Jong, K A and Scholten. R) John Wdey, New York, 67-96.

569 Evans, M. A., Bebout, G.E., Brown, C.H., 2012. Changing fluid conditions during folding: An example from
570 the central Appalachians. Tectonophysics 576–577, 99–115.

571 Evans, M. A., Fischer, M.P., 2012. On the distribution of fluids in folds: A review of controlling factors and
572 processes. J. Struct. Geol. 44, 2–24.

573 Evans, M., Battles, D., 1999. stable isotope analyses of veins from the central Appalachian Valley and Ridge
574 province: Implications for regional synorogenic hydrologic structure and fluid migration. Geol. Soc.
575 Am. Bull. 111, 1841–1860.

576 Ferket, H., Roure, F., Swennen, R., Ortuno, S., 2000. Fluid migration placed into the deformation history of
577 fold-and-thrust belts: an example from the Veracruz basin (Mexico). Journal of Geochemical
578 Exploration 69–70, 275–279.

579 Fischer, M.P., Higuera-Díaz, I.C., Evans, M. A., Perry, E.C., Lefticariu, L., 2009. Fracture-controlled
580 paleohydrology in a map-scale detachment fold: Insights from the analysis of fluid inclusions in
581 calcite and quartz veins. J. Struct. Geol. 31, 1490–1510.

582 Fischer, M.P., Jackson, P.B., 1999. Stratigraphic controls on eformation patterns in fault-related folds: a
583 detachment fold example from the Sierra Madre Oriental, northeast Mexico. J. Struct. Geol. 21, 613–
584 633.

585 Fischer, M.P., Wilkerson, M.S., 2000. Predicting the orientation of joints from fold shape□: Results of
586 pseudo – three-dimensional modeling and curvature analysis. Geology 28, 15–18.

587 Fitz-Diaz, E., Hudleston, P., Siebenaller, L., Kirschner, D., Camprubí, A., Tolson, G., Puig, T.P., 2011. Insights
588 into fluid flow and water-rock interaction during deformation of carbonate sequences in the
589 Mexican fold-thrust belt. J. Struct. Geol. 33, 1237–1253.

590 Gale, J.F.W., Reed, R.M., Holder, J., 2007. Natural fractures in the Barnett Shale and their importance for
591 hydraulic fracture treatments. Am. Assoc. Pet. Geol. Bull. 91, 603–622.

592 Hathaway, J. C., Degens, E.G., 1969. Methane-derived marine carbonates of Pleistocene age. Science 165,
593 690–692.

594 Hervouët, Y., Espurt, N., Dhont, D., 2005. Failles normales Paléocène à Lutétien en zone sud-pyrénéenne
595 (Aragon, Espagne) et flexuration de la plaque ibérique. Comptes Rendus Geoscience 337, 385–392.

596 Henderson, I.H.C., McCaig, A. M., 1996. Fluid pressure and salinity variations in shear zone-related veins,
597 central Pyrenees, France: Implications for the fault-valve model. Tectonophysics 262, 321–348.

598 Hilgers, C., Koehn, D., Bons, P.D., Urai, J.L., 2001. Development of crystal morphology during unitaxial
599 growth in a progressively widening vein□: II . Numerical simulations of the evolution of antitaxial
600 fibrous veins. Jou. Struc. Geol. 23, 873–885.

601 Hogan, P.J., Burbank, D.W., 1996. Evolution of the Jaca piggyback basin and emergence of the External
602 Sierras, southern Pyrenees. In: P.F. Friend and C.J. Dabrio (Editors), Tertiary Basins of Spain.
603 Cambridge Univ. Press, 153-160.

604 Huyghe, D., Mouthereau, F., Castelltort, S., Filleaudeau, P-Y., Emmanuel, L, 2009. Paleogene propagation of
605 the southern Pyrenean thrust wedge revealed by finite strain analysis in frontal thrust sheets:
606 implications for mountain building. Earth and Planetary Science Letters 288, 421-433.
607
608 Huyghe, D., Castelltort, S., Mouthereau, F., Serra-Kiel, J., Filleaudeau, P.-Y., Berthier, B., Emmanuel, L.,
609 Renard, M., 2012a. Large scale facies change in the middle Eocene South-Pyrenean foreland basin:
610 The role of tectonics and prelude to Cenozoic ice-ages. Sedimentary Geology 253-254, 25-46.
611
612 Huyghe, D., Mouthereau, F., Emmanuel, L., 2012b. Oxygen isotopes of marine mollusc shells record Eocene
613 elevation change in the Pyrenees. Earth and Planetary Science Letters 345-348, 131-141.
614
615 Jolivet, M., Labaume, P., Monie, P., Brunel, M., Arnaud, N., Campani, M., 2007. Thermochronology
616 constraints for the propagation sequence of the south Pyrenean basement thrust system (France-
617 Spain), Tectonics 26, TC5007, doi:10.1029/2006TC002080.

618 Katz, D. A., Eberli, G.P., Swart, P.K., Smith, L.B., 2006. Tectonic-hydrothermal brecciation associated with
619 calcite precipitation and permeability destruction in Mississippian carbonate reservoirs, Montana
620 and Wyoming. Am. Assoc. Pet. Geol. Bull. 90, 1803–1841.

621 Kim, S.-T., O'Neil, J.R., 1997. Equilibrium and nonequilibrium oxygen isotope effects in synthetic
622 carbonates. Geochim. Cosmochim. Acta 61, 3461–3475.

623 Lacombe O., Swennen R., Caracausi A. (eds), 2014. Thematic Issue :Fluid-rock-tectonics interactions in
624 basins and orogens. Marine and Petroleum Geology, 55, 1-332

625 Lacombe O, Tavani S., Soto R. (eds), 2012. Thematic Issue : Into the deformation history of folded rocks.
626 Tectonophysics, 576-577, 1-216

627 Lacombe O., 2012. Do fault slip data inversions actually yield 'paleostresses' that can be compared with
628 contemporary stresses ? A critical discussion. Comptes Rendus Geoscience 344, 159-173.

Lacombe, O., Bellahsen, N., Mouthereau, F., 2011. Fracture patterns in the Zagros Simply Folded Belt (Fars, Iran): constraints on early collisional tectonic history and role of basement faults. Geological Magazine, thematic issue « Geodynamic evolution of the Zagros », O. Lacombe, B. Grasemann and G. Simpson (eds), 148, 940-963.

Lacroix, B., Buatier, M., Labaume, P., Travé, a., Dubois, M., Charpentier, D., Ventalon, S., Convert-Gaubier, D., 2011. Microtectonic and geochemical characterization of thrusting in a foreland basin: Example of the South-Pyrenean orogenic wedge (Spain). Journal of Structural Geology 33, 1359–1377.

Lacroix, B., Travé, A., Buatier, M., Labaume, P., Vennemann, T., Dubois, M., 2014. Syntectonic fluid-flow along thrust faults: Example of the South-Pyrenean fold-and-thrust belt. Marine and Petroleum Geology 49, 84–98.

Laubach, S.E., Olson, J., Gross, M.R., 2009. Mechanical and fracture stratigraphy. AAPG Bulletin 93, 1413–1427.

Machel, H.G., 2000. Application of Cathodoluminescence to carbonate diagenesis. In: Pagel, M., Barbin, V., Blanc, P., Ohnenstetter, D. (eds.), Cathodoluminescence in Geosciences. Springer-Verlag, Heigelberg, Germany, 271-302.

Machel, H.G., Cavel, P.A., 1999. Low-flux, tectonically-induced squeegee fluid flow (« hot flash ») into the Rocky Mountain Foreland Basin. Bulletin of Canadian Petroleum Geology 47, 510-533.

McCaig, A.M., Tritlla, J., and Banks, D., 2000, Fluid flow patterns during Pyrenean thrusting. Journal of Geochemical Exploration 69-70, 539–543.

McCaig, A.M., Wayne, D.M., Marshall, J.D., Banks, D., Henderson, I., 1995. Isotopic and fluid inclusion studies of fluid movement along the Gavarnie Thrust, central Pyrenees: reaction front in carbonate mylonites. American Journal of Science 295, 309-343.

Millán, H., 1996. Estructura y cinematica del frente de cabalgamiento surpirenaico, Sierras Exteriores aragonesas, PhD Thesis, Universidad de Zaragoza, Spain, 330 pp.

Millán, H., Aurell, M., Meléndez, A., 1994. Synchronous detachment folds and coeval sedimentation in the Prepyrenean External Sierras (Spain): a case study for a tectonic origin of sequences and systems tracts. Sedimentology 41, 1001-1024.

Molina, E., Ortiz, N., Serra-Kiel, J., 1988. Implicationes paleoecologicas de los foraminiferos en el Eocene del Prepirineo oscense (sector de Arguís). Revista Espanola de Paleontologia 3, 45-57.

Morley, C.K., Warren, J., Tingay, M., Boonyasaknanon, P., and Julapour, A., 2014, Comparison of modern fluid distribution, pressure and flow in sediments associated with anticlines growing in deepwater (Brunei) and continental environments (Iran): Marine and Petroleum Geology, thematic issue on fluid-rock-tectonics interactions in basins and orogens. , Lacombe O., Swennen R., Caracausi A. (eds), 55, 230–249, doi: 10.1016/j.marpetgeo.2013.11.011.

Nalpas, T., Gapais, D., Verges, J., Barrier, L., Gestain, V., Leroux, G., Rouby,D., Kermarrec, J.J., 2003. Effects of rate and nature of synkinematic sedimentation on the growth of compressive structures constrained by analogue models and field examples. Geol. Soc. Lond. Spec. Publ. 208, 307–319.

Novoa, E., Suppe, J., Shaw, J.H., 2000. Inclined-shear resto- ration of growth folds. AAPG Bull. 84, 787–804.

Oliva-Urcia, B., Pueyo, E., 2007. Rotational basement kinematics deducted from remagnetized cover rocks (Internal Sierras, southwestern Pyrenees). Tectonics 26, TC4014, doi:10.1029/2006TC001955.

671 Poblet, J., Hardy, S., 1995. Reverse modelling of detachment folds; application to the Pico del Aguila
672 anticline in the South Central Pyrenees (Spain). Journal of Structural Geology 17, 12, 1707 – 1724.

673 Poblet, J., Muñoz, J., Travé, A., and Sierra-Kiel, J., 1998. Quantifying the kinematics of detachment folds
674 using three-dimensional geometry: Application to the Mediano anticline (Pyrenees, Spain). GSA
675 Bulletin 110, 111–12.

676 Pueyo, E.L., Millán, H., Pocoví, A., 2002. Rotation velocity of a thrust: a paleomagnetic study in the External
677 Sierras (Southern Pyrenees). Sedimentary Geology 146, 191-208.

678 Puigdefàbregas, C., 1975. La sedimentación molásica en la cuenca de Jaca. Pirineos 104, 1-188.

679 Pujalte, V., Baceta, J., Schmitz, B., Orue-Etxebarria, X., Payros, A., Bernaola, G., Apellaniz, E., Caballero, F.,
680 Robador, A., Serra-Kiel, J., Tosquella, J., 2009. Redefinition of the Ilerdian Stage (early Eocene).
681 Geologica Acta 7, 177–194.

682 Qing, H., Mountjoy, E., 1992. Large-scale fluid flow in the Middle Devonian Presqu'ile Barrier, Western
683 Canada sedimentary basin. Geology 20, 903–906.

684 Quintà, A., Tavani, S., 2012. The foreland deformation in the south-western Basque–Cantabrian Belt
685 (Spain).Tectonophysics, thematic issue : « Into the deformation history of folded rocks » , O.
686 Lacombe, S. Tavani, R. Soto (eds), , 576-577, 4-19.

687 Ramsay, J., 1980. The crack-seal mechanism of rock deformation. Nature 284, 135–139.

688 Reynolds, T.J., Goldstein, R.H., 1994. Systematics of fluid inclusions in diagenetic minerals, SEPM Short
689 Course.

690 Roedder, E., 1984. Fluid Inclusions. Rewiews in Mineralogy 12, 644 pp.

691 Rosenbaum, J., Sheppard, S.M.F., 1986. An isotopic study of side- rites, dolomites and ankerites at high
692 temperatures. Geochimica et Cosmochimica Acta 50, 1147–1150.

693 Roure, F., Swennen, R., Schneider, F., Faure, J.L., Ferket, H., Guilhaumou, N., Osadetz, K., Robion, P.,
694 Vandeginste, V., 2005. Incidence and Importance of Tectonics and Natural Fluid Migration on
695 Reservoir Evolution in Foreland Fold-And-Thrust Belts. Oil Gas Sci. Technol. 60, 67–106.

696 Savage, H.M., Ryan Shackleton, J., Cooke, M.L., Riedel, J.J., 2010. Insights into fold growth using fold-related
697 joint patterns and mechanical stratigraphy. J. Struct. Geol. 32, 1466–1475.

698 Sztràkos, K., Castelltort, S., 2001. La sédimentologie et les foraminifères bartoniens et priaboniens des
699 coupes d'Arguis (Prépyrénées aragonaises, Espagne). Incidence sur la corrélation des biozones à la
700 limite Bartonien/Priabonien. Revue de Micropaléontologie 44, 233-247.

701 Tavani, S., Storti, F., Fernández, O., Muñoz, J. a., Salvini, F., 2006. 3-D deformation pattern analysis and
702 evolution of the Añisclo anticline, southern Pyrenees. J. Struct. Geol. 28, 695–712.

703 Teixell, A., 1996. The Anso transect of the southern Pyrenees: basement and cover thrust geometries.
704 Journal of the Geological Society. 153, 301-310.

705 Travé, A., Calvet, F., Sans, M., Verges, J., and Thirlwall, M., 2000. Fluid history related to the Alpine
706 compression at the margin of the south-Pyrenean Foreland basin: the El Guix anticline.
707 Tectonophysics, 321, 73–102.

708 Travé, A., Labaume, P., and Vergés, J., 2007, Fluid systems in Foreland Fold-and-Thrust Belts: An overview
709 from the Southern Pyrenees. In: Lacombe, O., Lavé, J., Roure, F., and Vergés, J. eds,, Thrust Belts and
710 Foreland Basins : From Fold Kinematics to Hydrocarbons Systems, Springer, 93–115.

711 Van Geet, M., Swennen, R., Durmishi, C., Roure, F., Muchez, P.H., 2002. Paragenesis of Cretaceous to Eocene
712 carbonate reservoirs in the Ionian fold and thrust belt (Albania): relation between tectonism and
713 fluid flow. Sedimentology 49, 697–718.

714 Vandeginste, V., Swennen, R., Allaeys, M., Ellam, R.M., Osadetz, K., Roure, F., 2012. Challenges of structural
715 diagenesis in foreland fold-and-thrust belts: A case study on paleofluid flow in the Canadian Rocky
716 Mountains West of Calgary. Mar. Pet. Geol. 35, 235–251.

717 Vidal-Royo, O., Koyi, H. A., Muñoz, J.A., 2009. Formation of orogen-perpendicular thrusts due to mechanical
718 contrasts in the basal décollement in the Central External Sierras (Southern Pyrenees, Spain).
719 Journal of Structural Geology 31, 523–539.

720 Vidal-Royo, O., Cardozo, N., Muñoz, J.A.; Hardy, S., Maerten, L., 2012. Multiple mechanisms driving
721 detachment folding as deduced from 3D reconstruction and geomechanical restoration: the Pico del
722 Aguila anticline (External Sierras, Southern Pyrenees). Basin Research 24, 294-313.

723 Vidal-Royo, O., Munoz, J.A., Hardy, S., Koyi, H., Cardozo, N., 2013. Structural evolution of the Pico del Águila
724 anticline (external Sierras, southern Pyrenees) derived from sandbox, numerical and 3D structural
725 modelling Techniques. Geologica Acta 11, 1–26.

726 Zamarreño, I., Anadón, P., Utrilla, R., 1997. Sedimentology and isotopic composition of Upper Palaeocene
727 to Eocene non-marine stromatolites, eastern Ebro Basin, NE Spain. Sedimentology 44, 159–176.

728

Captions

Figure 1: A- Regional geological map of the Southern Central Pyrenees with location of the balanced cross-sections that cross the Pico del Aguila anticline (Huyghe et al., 2009); B- Stratigraphic column for the Pico del Aguila area (after Castelltort et al., 2003). Lithological key of patterns from bottom to top: carets – evaporate, dashs – clay, parallelograms – dolostone, rectangles – limestone, big dots in irregular shapes – river conglomerates, plain black – marls, fine dots - sandstone; C- Transverse and longitudinal regional cross-sections in the Sierras Exteriores, focusing on the Pico del Aguila Area (Huyghe et al., 2009).

Figure 2: Geological map of the Pico del Aguila Anticline based on previously published maps (Puigdefabregas, 1975; Millán, 1996; Vidal-Royo et al., 2012), aerial photographs and new field observation and measurements. A balanced cross-section following line C-C' is presented, with a length balance of layers for strata younger than Triassic and an area balance for the Triassic rocks of the décollement. Dotted frames on the maps are areas of maps presented in figures 4-6. White-labeled black dots locate fracture measurement sites or sample sites for geochemical analyses. Please refer to supplementary material 2 for GPS values. In the stratigraphy caption box, "cont." refers to continental environment.

Figure 3: Photomicrographs of thin- and thick-sections using polarized and cross-polaryzed microscopy. a – Multiple crack-seals and fibrous vein where calcite crystals exhibit the growth direction, recording a mixed mode I-mode II 'transtensional' opening mode of the vein (sample A14); b – Vein with elongated blocky calcite texture where the grain growth direction is perpendicular to the border of the vein, indicating a mode I opening (sample A44). c – Photomicrograph of fluid inclusions in a thick-section. Biggest primary or pseudo-secondary fluid inclusions are circled in red and the stained parts in crystals corresponds to an increase in density of secondary fluid inclusion trails (sample A45). d – Calcite vein with blocky texture fringed by microsparitic crystals, recording a two-stage opening of the vein (sample A86), analogous to the crack-seal model (Ramsay, 1980).

Figure 4: Results of fracture analysis in the Triassic to Lutetian prefolding strata in the anticline. Results are presented on 3 diagrams (Schmidt' lower-hemisphere, equal-area stereonets) displaying raw data in current strata attitude (left), then corrected for fold axial plunge related to the Gavarnie thrust activation (middle), and corrected for local bedding dip (right). Location of the measurement area is given in Fig. 2 and in supplementary material 2. Abbreviations on the map are for the formations: Ar – Arguis Fm., Gu – Guara Fm., Tp – Tremp Fm., A-B – Adraen Bona Fm., Tr – Triassic Fms.

Figure 5: Results of fracture analysis in the western syncline located in the Pico del Aguila area. Same key as in Fig. 4. Abbreviations on the map are for formations: Ar – Arguis Fm., Gu – Guara Fm., Tp – Tremp Fm., A-B – Adraen Bona Fm.

Figure 6: Results of fracture analysis in the syn-folding and post-folding strata of Bartonian to Priabonian age, respectively. Same key as in Fig. 4. Abbreviations on the map are for formations: Cp – Campodarbe Fm., B-A – Beslusé Atares Fm., Ar – Arguis Fm., Gu – Guara Fm.

Figure 7: Results of fault-slip inversion (Schmidt' stereonets lower hemisphere). Computed stress axes are reported as stars with three branches (σ_1), four branches (σ_2) and five branches (σ_3). Convergent/divergent black arrows indicate the direction of compression/tension. Results are represented in the current attitude of strata, and diagrams labeled as "corrected" correspond to the same computed tensor and fault-slip data but corrected for removal of fold axial plunge related to the activation of Gavarnie thrust. Diagrams labeled as "unbasc" are corrected for fold axis plunge then for bed tilt. Diagrams are gathered according to consistency of reconstructed paleostress tensors. Abbreviations on the map are for formations: Cp – Campodarbe Fm., B-A – Belsué Atares Fm., Ar – Arguis Fm., Gu – Guara Fm., Tp – Tremp Fm., A-B – Adraen Bona Fm., Tr – Triassic Fms.

Figure 8: a-d – Field photographs with chronological interpretations of fracture networks. Sites for photographs: site 39(a), site 497 (b), site 476 (c), and site 447(d). e-f – Photographs of faults and fractures showing the spacing and vertical persistence of fractures observed at site 433 (refer to Figs. 4 to 7 for location).

794

795 Figure 9: Photomicrographs of thin sections under cathodoluminescence microscopy: a
796 – Heterogeneous blocky-type calcite in vein, with brightness variation related to crystal
797 boundaries or to atomic-scale defects (sample A77); b - Heterogeneous blocky-type
798 calcite in vein exhibiting bright to dull orange zonation related to crystal growth (sample
799 A37); c – Elongated blocky-type calcite in vein exhibiting brightness variation related to
800 crystals (sample A44, Fig. 3-b). Please refer to the electronic version for colors.
801

802 Figure 10: Results of $\delta^{18}O$ and $\delta^{13}C$ analysis of veins and host-rocks displayed in context
803 of fracture age with respect to folding. a - $\delta^{18}O$ vs $\delta^{13}C$ plot, b - $\delta^{18}O$ of veins vs $\delta^{18}O$ of
804 related host-rocks. On all charts, solid symbols are for vein cements and fault coatings,
805 whereas empty symbol are for related host-rocks samples. Please refer to the text for
806 the explanation of labels *(1)* to *(4)*. All values are expressed in ‰PDB. Labels XX/YY
807 refers to the number of analyzes performed / number of samples collected. See Table 2
808 and Supplementary Table S1 for detailed isotopic data.
809

810 Figure 11: Schematic block diagrams of structural, sedimentary and mesostructural
811 evolutionary scenario of the Pico del Aguila anticline. Fracture sets and related
812 contractional/extensional trends are illustrated. Stratigraphic timing and timing with
813 respect to folding stated for each block diagram. Fractures are not represented
814 according to abundance. Labels (1) to (5) are related to local and regional stress
815 orientations (see text).
816

817 Figure 12: a - Schematic cross-section illustrating evolution of the paleo-fluid system in
818 the Pico del Aiguila Anticline. b - Comparison with the Sheep Mountain anticline,
819 Wyoming, USA (after Beaudoin et al., 2011; Evans and Fischer, 2012).
820

821 Table 1: Results of the statistical interpretation of fracture set orientation, stratigraphic
822 distribution and indicators for relative chronology.
823

824 Table 2: Number of samples used for isotopic analysis in each formation, along with the
825 related range of isotopic values measured.

826

827 Table S1: Results of isotopic analyses.

828 Table S2: Geographical location of samples and measurement sites

829

Set name	Set strike*	Set inclination	Stratigraphic units	Evidence for relative age
J1	120	bed-normal	Guara - lower Arguis	RD, CC, A
J2	90	bed-normal	Guara	RD, CC, A
J3	70	bed-normal	All	CC, A
J4	40	bed-normal	All	CC, A
J5	170	sub bed-normal	All	CC, A

*: mean strike within 10° computed statistically

RD: Restricted to Stratigraphic units CC: cross-cutting relationships; A: respect andersonian criterion

Age relative to folding	Formation		number of analyses/number of samples	Range of isotopic values (>80% samples)	
				$\delta^{18}O$ (‰PDB)	$\delta^{13}C$ (‰PDB)
Post-folding	Campodarbe	veins	7/8	-2.20 to -0.02	-1.77 to -0.77
		host-rock	7/8	-6.05 to -5.4	-1.2 to 0.05
Syn-folding	Belsue Atares	veins	2/3	-4.65 to -2.91	-2.61 to -1.38
		host-rock	3/3	-5.81 to -4.81	-1.53 to 0.11
	Arguis	veins	25/25	-4.35 to -0.66	-1.64 to 0.48
		host-rock	20/25	-4.47 to -2.55	-1.7 to 0.43
	Guara	veins	29/29	-10.4 to -1.42	-0.05 to 2.25
		host-rock	20/29	-6.7 to -1.42	-1.5 to 2.15
Pre-folding	Tremp	veins	3/3	-7.26 to -6.71	-7.77 to -6.34
		host-rock	1/3	-3.77	-6.29
	Adraen Bona	veins	1/1	-5.43	-0.56
		host-rock	1/1	-3.9	1.49
	Triassic	veins	3/4	-7.65 to -6.73	-5.43 to -3.51
		host-rock	4/4	-5.78 to -3.28	-1.37 to 2.65

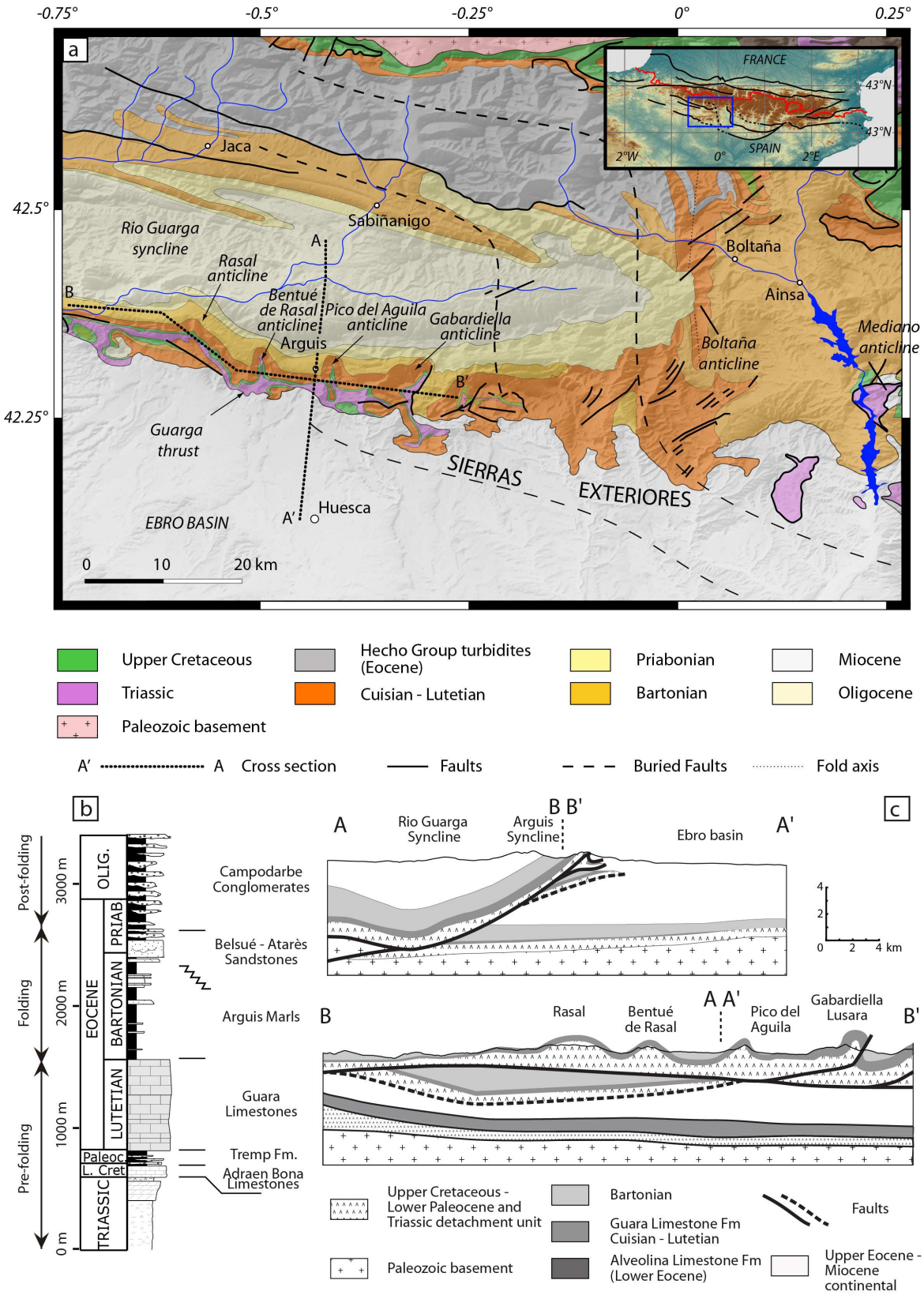
-0.75°
-0.5°
-0.25°
0°
0.25°
42.5°
42.25°
a
FRANCE
SPAIN
43°N
2°W
0°
2°E
Jaca
Sabiñanigo
Boltaña
Ainsa
Rio Guarga syncline
Rasal anticline
Bentué de Rasal anticline
Pico del Aguila anticline
Gabardiella anticline
Arguis
Boltaña anticline
Mediano anticline
Guarga thrust
SIERRAS EXTERIORES
EBRO BASIN
Huesca
A
A'
B
B'
0 10 20 km
Upper Cretaceous
Triassic
Paleozoic basement
Hecho Group turbidites (Eocene)
Cuisian - Lutetian
Priabonian
Bartonian
Miocene
Oligocene
Cross section
Faults
Buried Faults
Fold axis
b
Post-folding
Folding
Pre-folding
3000 m
2000 m
1000 m
0 m
OLIG.
PRIAB
BARTONIAN
EOCENE
LUTETIAN
Paleoc.
L. Cret
TRIASSIC
Campodarbe Conglomerates
Belsué - Atarès Sandstones
Arguis Marls
Guara Limestones
Tremp Fm.
Adraen Bona Limestones
c
Rio Guarga Syncline
Arguis Syncline
Ebro basin
4 km
Rasal
Bentué de Rasal
Pico del Aguila
Gabardiella Lusara
Upper Cretaceous - Lower Paleocene and Triassic detachment unit
Paleozoic basement
Bartonian
Guara Limestone Fm Cuisian - Lutetian
Alveolina Limestone Fm (Lower Eocene)
Faults
Upper Eocene - Miocene continental

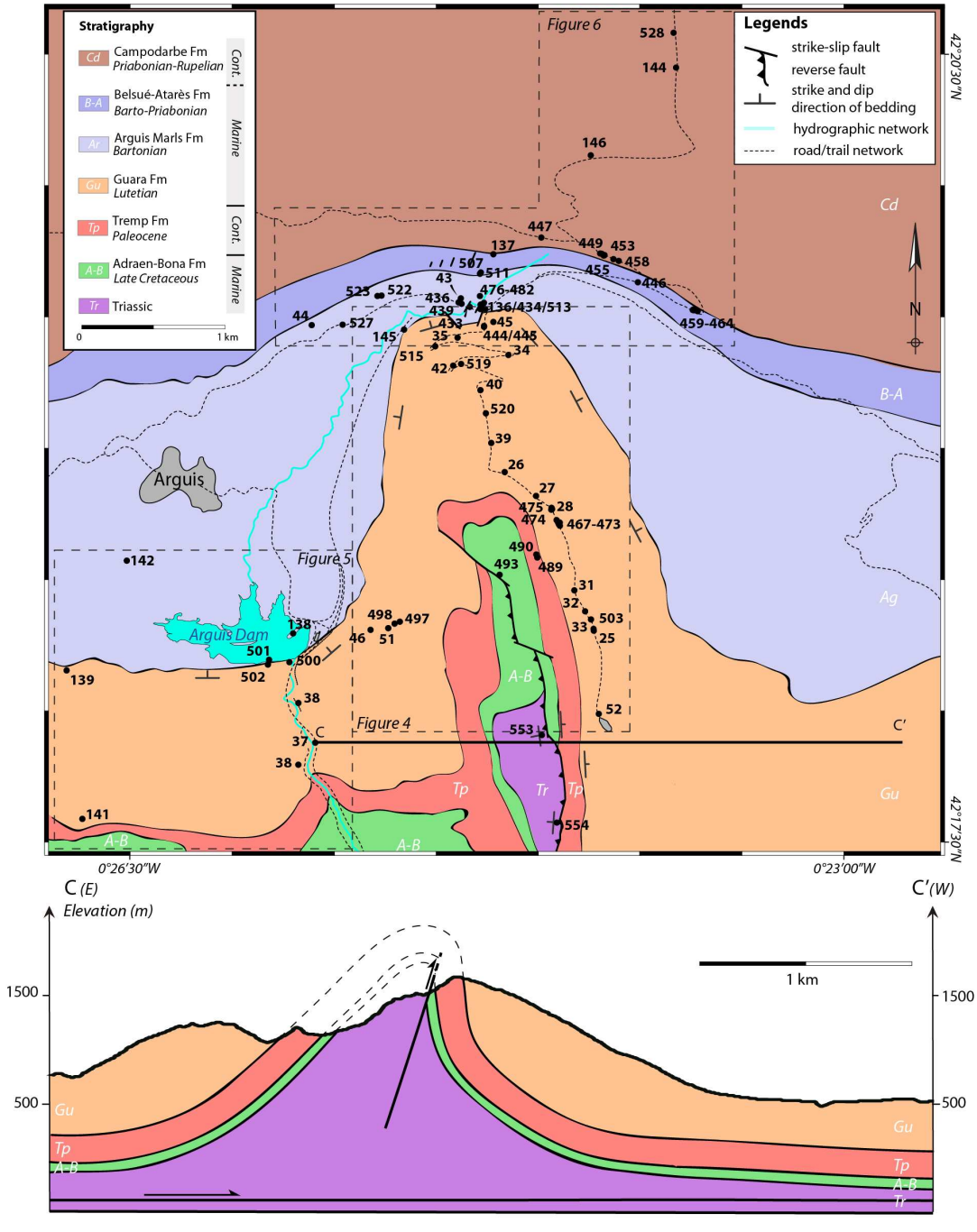
Stratigraphy
Cd Campodarbe Fm Priabonian-Rupelian
B-A Belsué-Atarès Fm Barto-Priabonian
Ar Arguis Marls Fm Bartonian
Gu Guara Fm Lutetian
Tp Tremp Fm Paleocene
A-B Adraen-Bona Fm Late Cretaceous
Tr Triassic
Cont.
Marine
0
1 km
Legends
strike-slip fault
reverse fault
strike and dip direction of bedding
hydrographic network
road/trail network
Figure 6
Figure 5
Figure 4
Arguis
Arguis Dam
N
42°20'30"N
42°17'30"N
0°26'30"W
0°23'00"W
C (E)
C' (W)
Elevation (m)
1500
500
1 km

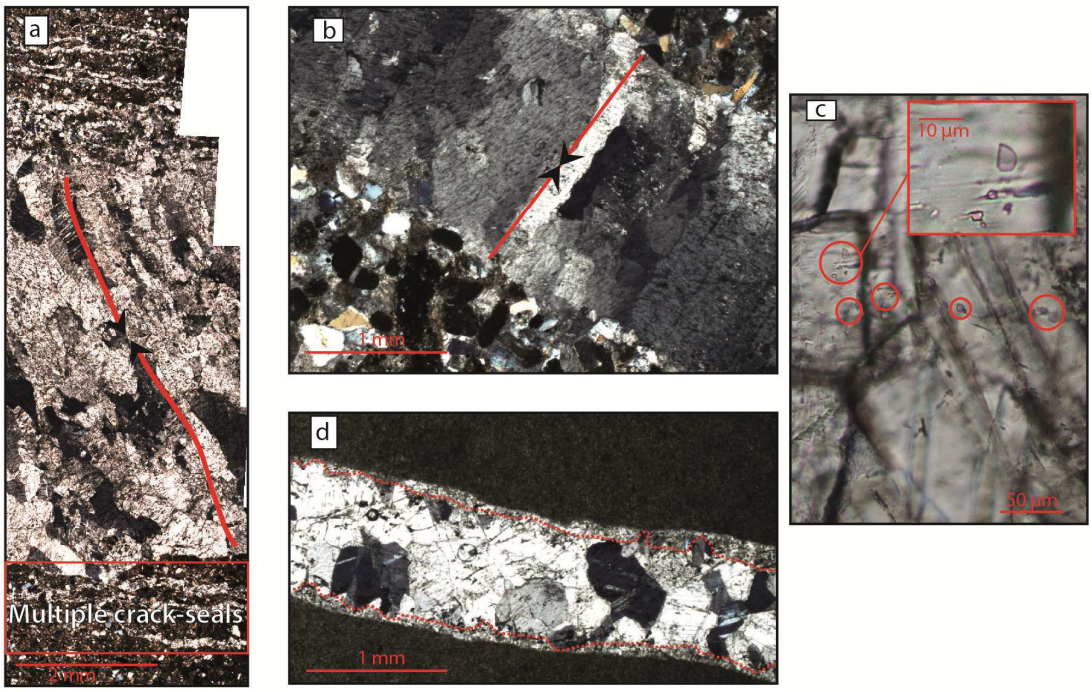

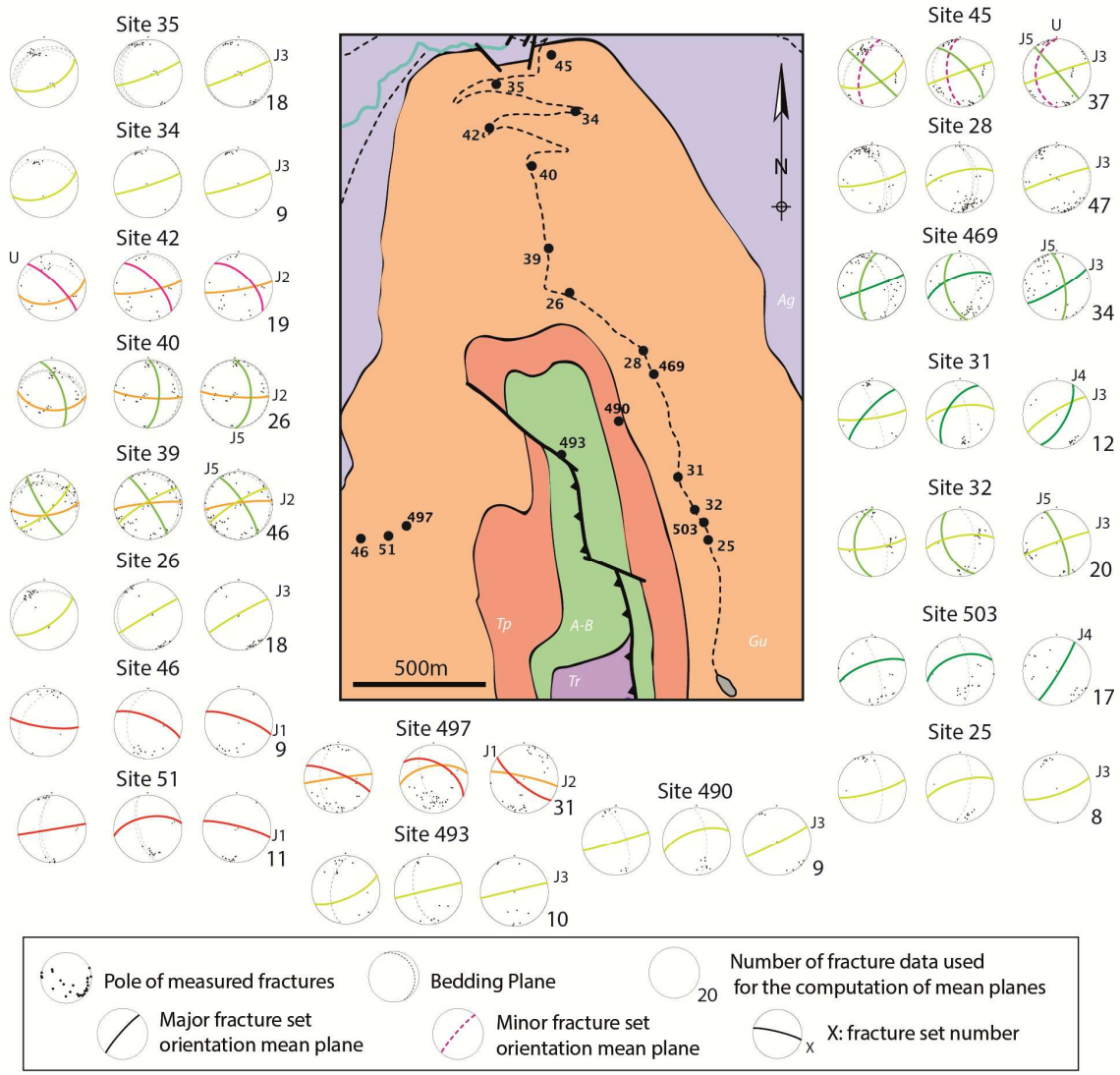
Site 35
J3
18
Site 34
J3
9
Site 42
U
J2
19
Site 40
J2
J5
26
Site 39
J5
J2
46
Site 26
J3
18
Site 46
J1
9
Site 51
J1
11
45
35
34
42
40
39
26
28
469
490
493
31
32
503
25
497
46
51
N
Ag
Tp
A-B
Tr
Gu
500m
Site 497
J1
J2
31
Site 493
J3
10
Site 490
J3
9
Site 45
U
J5
J3
37
Site 28
J3
47
Site 469
J5
J3
34
Site 31
J4
J3
12
Site 32
J5
J3
20
Site 503
J4
17
Site 25
J3
8
Pole of measured fractures
Bedding Plane
20
Number of fracture data used for the computation of mean planes
Major fracture set orientation mean plane
Minor fracture set orientation mean plane
X
X: fracture set number

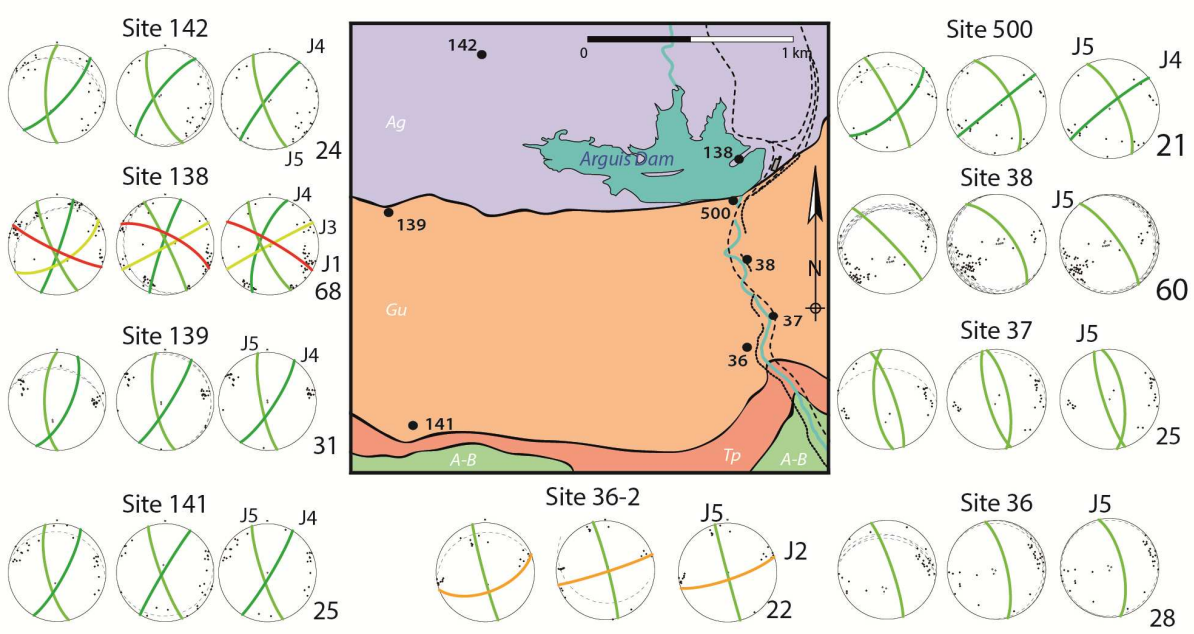

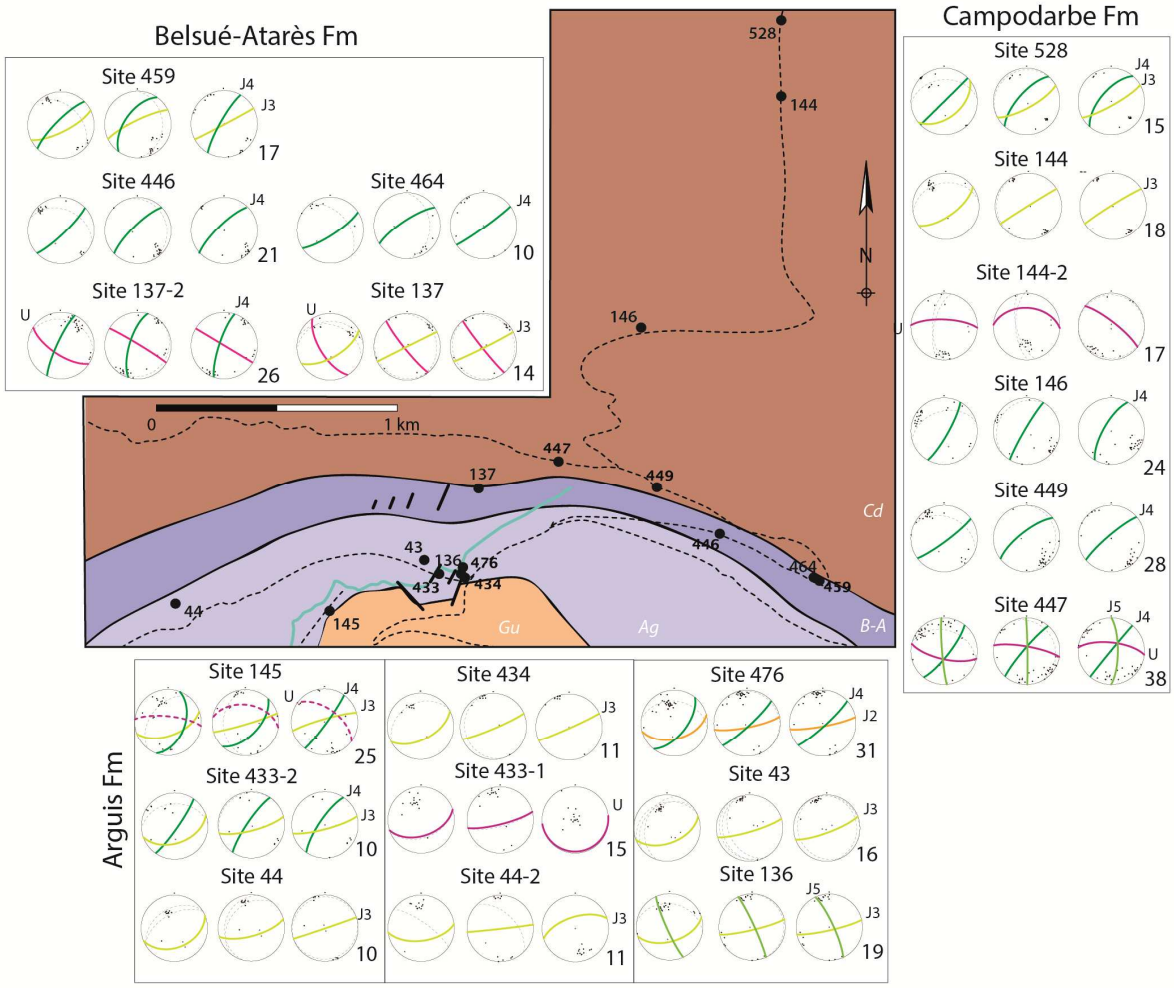

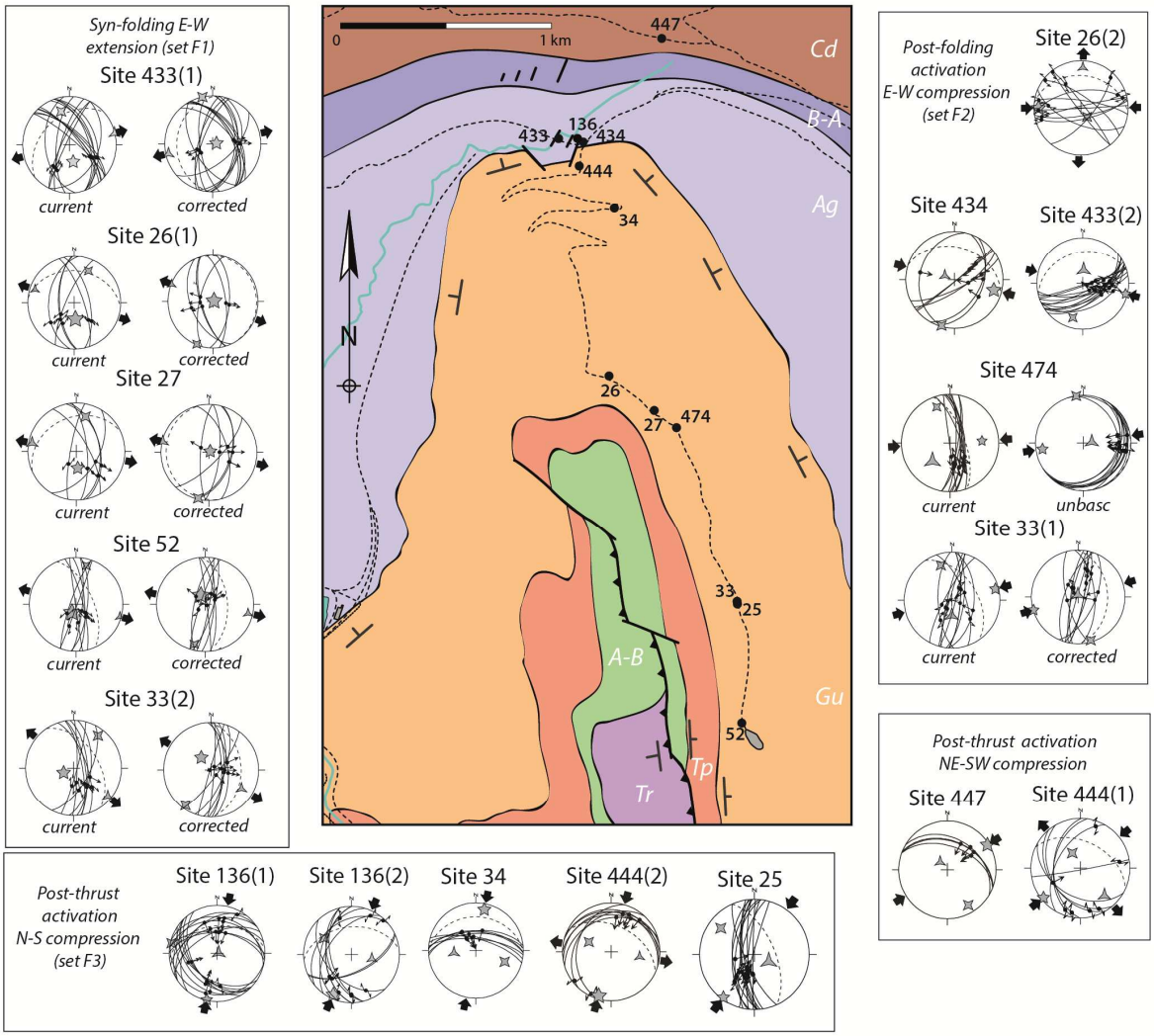
Syn-folding E-W extension (set F1)
Site 433(1)
current
corrected
Site 26(1)
current
corrected
Site 27
current
corrected
Site 52
current
corrected
Site 33(2)
current
corrected
0
1 km
447
Cd
B-A
136
433
434
444
Ag
34
N
26
27
474
33
25
A-B
Gu
52
Tp
Tr
Post-folding activation E-W compression (set F2)
Site 26(2)
Site 434
Site 433(2)
Site 474
current
unbasc
Site 33(1)
current
corrected
Post-thrust activation NE-SW compression
Site 447
Site 444(1)
Post-thrust activation N-S compression (set F3)
Site 136(1)
Site 136(2)
Site 34
Site 444(2)
Site 25

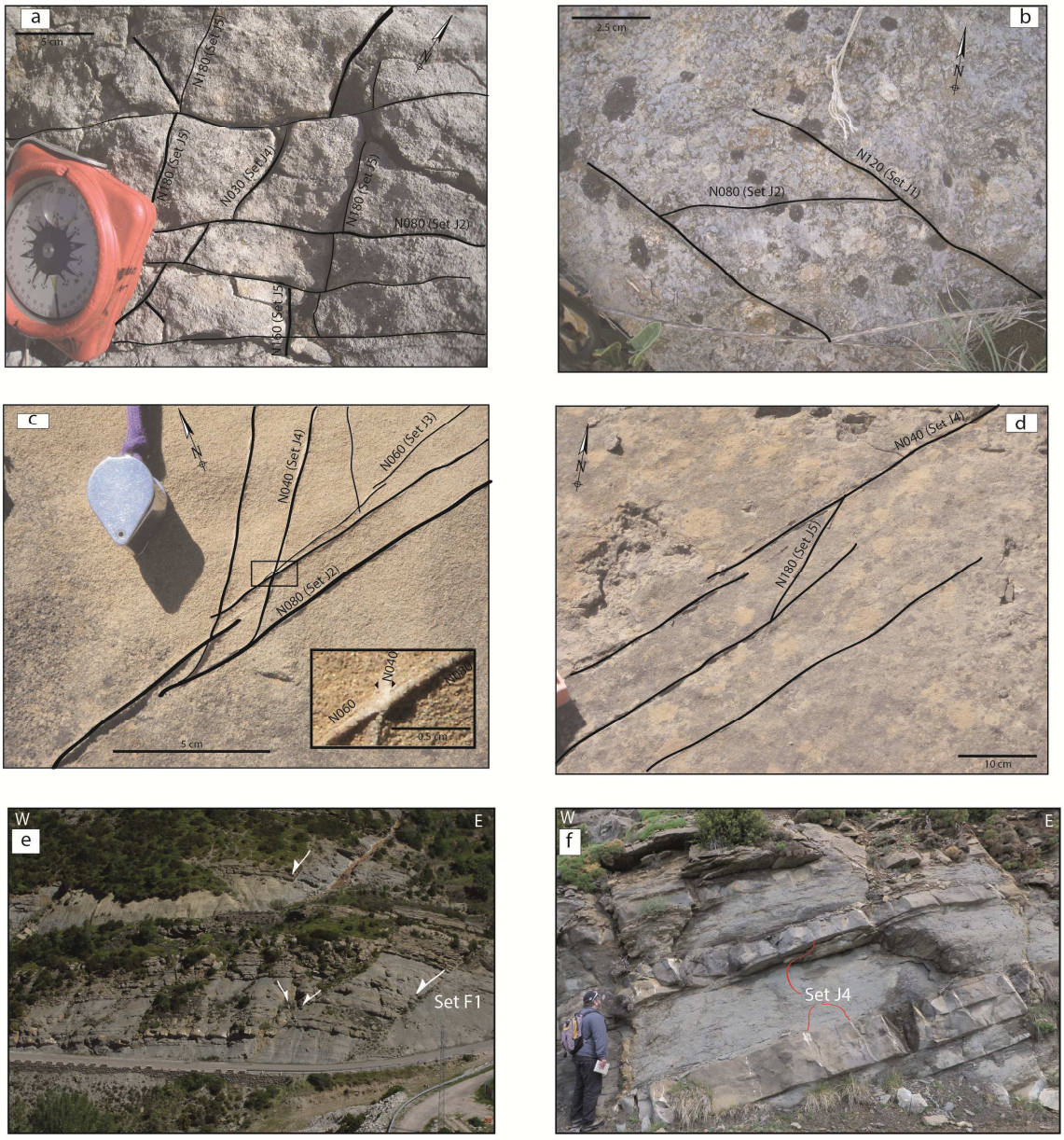
a
N180 (Set J5)
N030 (Set J4)
N080 (Set J2)
b
2.5 cm
N120 (Set J1)
N080 (Set J2)
c
N040 (Set J4)
N060 (Set J3)
N080 (Set J2)
5 cm
d
N040 (Set J4)
N180 (Set J5)
10 cm
W
E
e
Set F1
f
Set J4

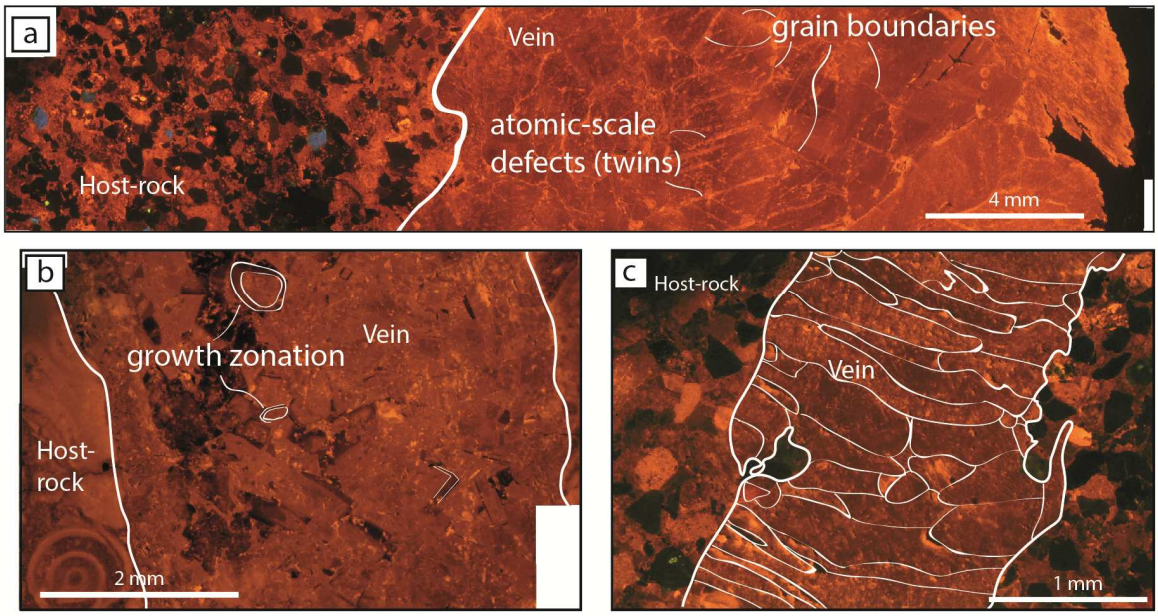

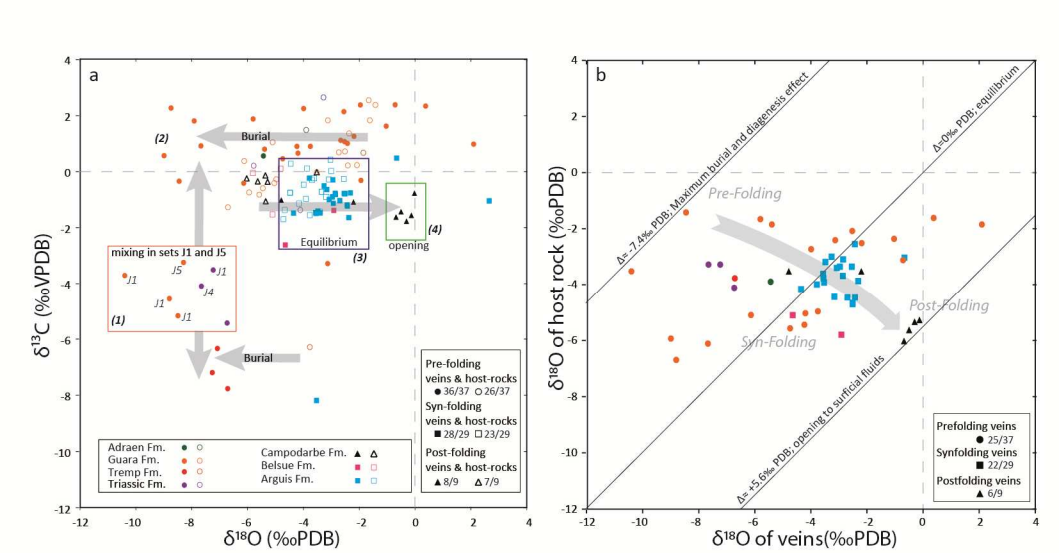

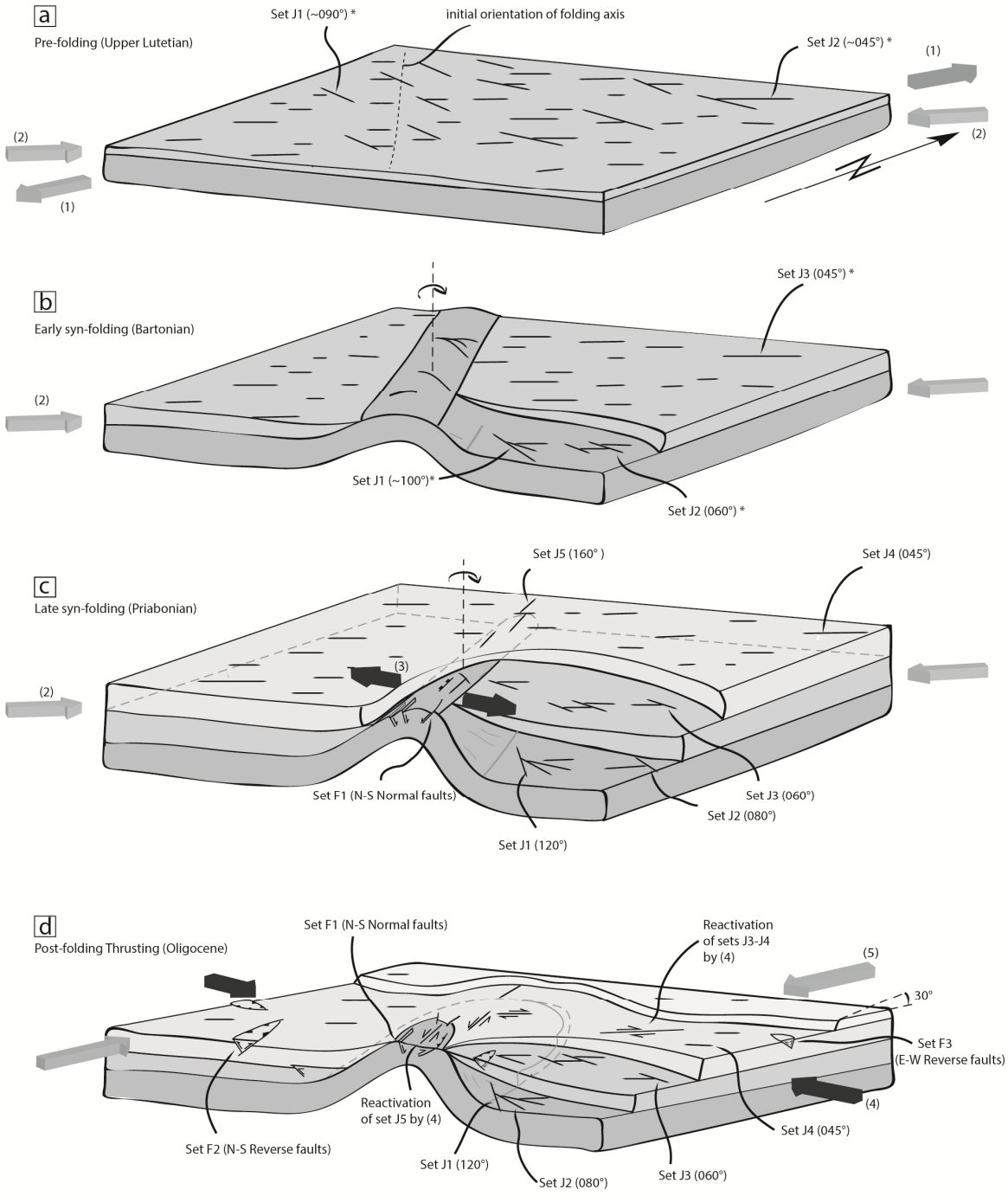
a
Pre-folding (Upper Lutetian)
Set J1 (~090°) *
initial orientation of folding axis
Set J2 (~045°) *
(1)
(2)
(2)
(1)
b
Early syn-folding (Bartonian)
Set J3 (045°) *
(2)
Set J1 (~100°)*
Set J2 (060°) *
c
Late syn-folding (Priabonian)
Set J5 (160°)
Set J4 (045°)
(3)
(2)
Set F1 (N-S Normal faults)
Set J3 (060°)
Set J2 (080°)
Set J1 (120°)
d
Post-folding Thrusting (Oligocene)
Set F1 (N-S Normal faults)
Reactivation
of sets J3-J4
by (4)
(5)
30°
Set F3
(E-W Reverse faults)
(4)
Reactivation
of set J5 by (4)
Set J4 (045°)
Set F2 (N-S Reverse faults)
Set J1 (120°)
Set J2 (080°)
Set J3 (060°)

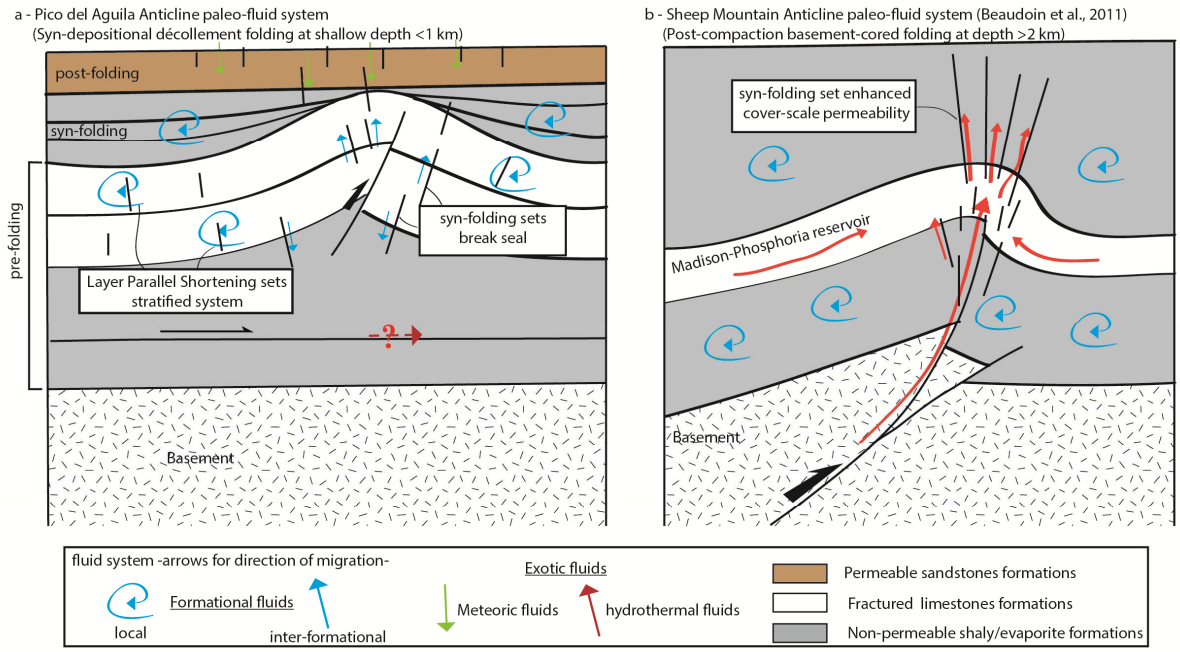

Highlights:

. Fluid system deciphered during syn-sedimentary folding
. Role of tectonic and sedimentary environment on fluid system evolution
. Role of burial on vertical permeability of fractures
. Fracture development witnesses fold rotation around a vertical axis

Deposition regarding folding	Sample	Formation	Age	Fracture Set	Vein isotopic ratios		Host rock isotopic ratio		Site Number (Figure for location)
					$\partial^{18}O$	$\partial^{13}C$	$\partial^{18}O$	$\partial^{13}C$	
Post-folding	A040	Campodarbe	Priabonian	Set J4			-5.36	-0.13	447 (Fig. 6)
	A041	Campodarbe	Priabonian	Set J5	-0.3	-1.77	-5.35	-1.06	449 (Fig. 6)
	A042	Campodarbe	Priabonian	Set J5	-0.68	-1.62	-6.03	-0.24	450 (Fig. 6)
	A044	Campodarbe	Priabonian	Set J4	-0.13	-1.56	-5.28	-0.36	452 (Fig. 6)
	A045	Campodarbe	Priabonian	Set J4	-0.5	-1.43	-5.64	-0.34	453 (Fig. 6)
	A048	Campodarbe	Priabonian	Set J3	-0.02	-0.77			455 (Fig. 6)
	A050	Campodarbe	Priabonian	Set J4	-2.2	-1.08	-3.52	-0.02	458 (Fig. 6)
	A050	Campodarbe	Priabonian	Set J2	-4.79	-1.02	-3.52	-0.02	458 (Fig. 6)
Syn-folding	A103	Belsue-Atarès	Bartonian	Set J3			-4.81	0.11	507 (Fig. 4)
	A054	Belsue-Atarès	Bartonian	Set J3	-2.91	-1.38	-5.81	-0.05	465 (Fig. 4)
	A104	Belsue-Atarès	Bartonian	Set J2	-4.65	-2.61	-5.11	-1.53	511 (Fig. 4)
	A001	Arguis	Bartonian	Set J2	-3.48	-1.41	-3.19	-0.9	433 (Fig. 4)
	A003	Arguis	Bartonian	Set F1	-3.53	-8.19	-3.91	-0.97	433 (Fig. 7)
	A004	Arguis	Bartonian	Set F1	-3.4	-1.47			433 (Fig. 7)
	A005	Arguis	Bartonian	Set F1	-3.55	-1.49	-3.77	-1.55	433 (Fig. 7)
	A008	Arguis	Bartonian	Set J3	-4.35	-1.48	-4.16	-1.14	433 (Fig. 4)
	A009	Arguis	Bartonian	Set F1	2.66	-1.04			433 (Fig. 7)
	A010	Arguis	Bartonian	Set F1	-3.26	-0.51	-3	0.02	433 (Fig. 7)
	A011	Arguis	Bartonian	Set J2	-2.31	-0.76	-3.87	0.12	433 (Fig. 4)
	A012	Arguis	Bartonian	Set F1	-2.54	-0.78	-3.35	-0.72	433 (Fig. 7)
	A013	Arguis	Bartonian	Set J2	-2.51	-0.78	-4.72	-1.7	433 (Fig. 4)
	A013	Arguis	Bartonian	Set J2	-2.51	-0.78	-4.67	-1.37	433 (Fig. 4)
	A015	Arguis	Bartonian	Set J1	-2.94	-0.29			434 (Fig. 4)
	A020	Arguis	Bartonian	Set J4	-3.79	-0.23	-3.99	-0.46	436 (Fig. 4)
	A021	Arguis	Bartonian	Set J3	-2.86	-0.77	-3.69	-0.29	436 (Fig. 4)
	A022	Arguis	Bartonian	Set F2	-2.96	-0.9	-3.35	-0.72	439 (Fig. 7)
	A071	Arguis	Bartonian	Set J2	-3.56	-1.46	-3.61	-0.23	476 (Fig. 4)
	A072	Arguis	Bartonian	Set J2	-2.43	-1.19	-2.55	-0.26	476 (Fig. 4)
	A073	Arguis	Bartonian	Set J3	-2.85	-0.82	-3.09	-0.28	477 (Fig. 4)
	A077	Arguis	Bartonian	Set J2	-2.7	-1.04	-4.47	-0.75	482 (Fig. 4)
	A077	Arguis	Bartonian	Set J3	-2.43	-1.23	-4.47	-0.75	482 (Fig. 4)
	A078	Arguis	Bartonian	Set J3	-2.37	-1.64			482 (Fig. 4)
	A107	Arguis	Bartonian	Set J3	-2.93	-1.13			513 (Fig. 4)
	A121	Arguis	Bartonian	Set F3	-0.66	0.48	-3.03	0.43	522 (Fig. 7)
	A124	Arguis	Bartonian	Set F2	-3.16	-0.64	-4.45	0.28	523 (Fig. 7)
	A128	Arguis	Bartonian	Set J2	-3.08	-1.00	-3.4	-1.44	527 (Fig. 4)
Pre-folding	A031	Guara	Lutetian	Set F2	-5.8	1.88	-1.66	2.55	444 (Fig. 7)
	A032	Guara	Lutetian	Set F3	-8.45	-0.34	-1.42	2.38	445 (Fig. 7)
	A033	Guara	Lutetian	Set F3	-3.99	2.25	-2.73	0.69	445 (Fig. 7)
	A037	Guara	Lutetian	Set J2	0.38	2.34	-1.62	1.83	445 (Fig. 4)
	A056	Guara	Lutetian	Set J3	-8.99	0.57	-5.94	-0.74	467 (Fig. 4)
	A057	Guara	Lutetian	Set J5	-4.19	0.66	-5.04	-0.41	467 (Fig. 4)
	A060	Guara	Lutetian	Set J5	-4.23	0.9	-5.45	-0.59	467 (Fig. 4)
	A060	Guara	Lutetian	Set J5	-3.75	0.9	-4.97	-0.27	467 (Fig. 4)
	A061	Guara	Lutetian	Set J5	-4.74	0.46	-5.58	-0.82	469 (Fig. 4)
	A064	Guara	Lutetian	Set J2	-2.52	1.07	-2.08	0.23	470 (Fig. 4)
	A064	Guara	Lutetian	Set J2	-2.66	1.12			470 (Fig. 4)
	A064	Guara	Lutetian	Set J5	-8.29	-3.24			470 (Fig. 4)
	A066	Guara	Lutetian	Set J3	-2.42	1.01			472 (Fig. 4)
	A066	Guara	Lutetian	Set J3	-1.94	-0.31			472 (Fig. 4)
	A067	Guara	Lutetian	Set J1	-10.4	-3.71	-3.52	-0.02	473 (Fig. 4)
	A068	Guara	Lutetian	Set J3	-1.03	1.62	-2.36	1.36	474 (Fig. 4)
	A070	Guara	Lutetian	Set J3	-2.19	1.26	-2.51	0.72	475 (Fig. 4)
	A087	Guara	Lutetian	Set J5	-6.14	-0.41	-5.1	1.05	497 (Fig. 4)
	A088	Guara	Lutetian	Set J1	-8.49	-5.17			497 (Fig. 4)
	A089	Guara	Lutetian	Set J3	-7.91	1.81			498 (Fig. 4)
	A091	Guara	Lutetian	Set J2	-7.67	0.92	-6.12	0.38	503 (Fig. 4)
	A094	Guara	Lutetian	Set J1	-8.8	-4.56	-6.7	-1.27	499 (Fig. 4)
	A097	Guara	Lutetian	???	-3.13	-3.28	-2.41	0.22	503 (Fig. 4)
	A100	Guara	Lutetian	???	-5.39	0.8	-1.85	0.67	503 (Fig. 4)
	A100	Guara	Lutetian	Set J2	2.1	0.98	-1.85	0.67	503 (Fig. 4)
	A109	Guara	Lutetian	Set J3	-0.71	2.38	-3.12	1.83	515 (Fig. 4)
	A115	Guara	Lutetian	Set J3	-8.74	2.27			519 (Fig. 4)
	A118	Guara	Lutetian	Set J5	-1.96	2.38			520 (Fig. 4)
	A119	Guara	Lutetian	???	-2.55	2.14			520 (Fig. 4)
	A086	Adraen-Bona	Cretaceous	Set J2	-5.43	0.56	-3.9	1.49	493 (Fig. 4)
	A082	Tremp	Cretaceous	Set J5	-7.08	-6.34			489 (Fig. 4)
	A083	Tremp	Cretaceous	Set J5	-7.26	-7.2			489 (Fig. 4)
	A084	Tremp	Cretaceous	Set J4	-6.71	-7.77	-3.77	-6.29	490 (Fig. 4)
	A131	Triassic	Triassic	Set J1	-7.23	-3.51	-3.28	2.65	553 (Fig. 4)
	A131	Triassic	Triassic	Set J4	-7.65	-4.09	-3.28	2.65	553 (Fig. 4)
	A132	Triassic	Triassic	???	-6.73	-5.43	-4.11	-1.37	555 (Fig. 4)
	A133	Triassic	Triassic				-5.78	0.21	555 (Fig. 4)

Accuracy of the measurments reported in this table is based on the standard deviation of the values obtained from the standards, and is of 0.05‰ for carbon and 0.1‰ for oxygen

Supplementary material 2: Site number lo cation

Site number	Longitude (decimal)	Latitude (decimal)	Formation	Age
446	-0.398945	42.327804	Campodarbe	Priabonian
447	-0.407133	42.330704	Campodarbe	Priabonian
449	-0.402130	42.329652	Campodarbe	Priabonian
450	-0.401991	42.329628	Campodarbe	Priabonian
452	-0.401818	42.329522	Campodarbe	Priabonian
453	-0.401759	42.329546	Campodarbe	Priabonian
455	-0.401005	42.329284	Campodarbe	Priabonian
458	-0.400551	42.329169	Campodarbe	Priabonian
528	-0.393591	42.342126	Campodarbe	Priabonian
459	-0.393884	42.325935	Belsué-Atarès	Bartonian
464	-0.394159	42.325990	Belsué-Atarès	Bartonian
465	-0.394251	42.326038	Belsué-Atarès	Bartonian
507	-0.412320	42.328541	Belsué-Atarès	Bartonian
511	-0.412357	42.328458	Belsué-Atarès	Bartonian
43	-0.414050	42.326917	Arguis	Bartonian
44	-0.426783	42.325333	Arguis	Bartonian
433	-0.413300	42.326370	Arguis	Bartonian
434	-0.411983	42.326212	Arguis	Bartonian
436	-0.414191	42.326608	Arguis	Bartonian
439	-0.414035	42.326563	Arguis	Bartonian
476	-0.412080	42.326619	Arguis	Bartonian
477	-0.412371	42.326508	Arguis	Bartonian
482	-0.412419	42.327050	Arguis	Bartonian
513	-0.412389	42.326222	Arguis	Bartonian
522	-0.420804	42.327150	Arguis	Bartonian
523	-0.421153	42.327128	Arguis	Bartonian
527	-0.424152	42.325338	Arguis	Bartonian
25	-0.40305	42.305800	Guara	Lutetian
26	-0.40723	42.314360	Guara	Lutetian
27	-0.407833	42.314367	Guara	Lutetian
28	-0.406483	42.313517	Guara	Lutetian
31	-0.404667	42.308367	Guara	Lutetian
32	-0.403767	42.307033	Guara	Lutetian
33	-0.403067	42.305917	Guara	Lutetian
34	-0.410050	42.323300	Guara	Lutetian
35	-0.414367	42.324433	Guara	Lutetian
36	-0.428350	42.297539	Guara	Lutetian
37	-0.426886	42.298922	Guara	Lutetian
38	-0.428286	42.301444	Guara	Lutetian
39	-0.411600	42.317750	Guara	Lutetian
40	-0.412467	42.321100	Guara	Lutetian
42	-0.414767	42.322667	Guara	Lutetian
45	-0.411300	42.325400	Guara	Lutetian
46	-0.422067	42.306017	Guara	Lutetian
51	-0.409400	42.309736	Guara	Lutetian
52	-0.402764	24.300739	Guara	Lutetian
136	-0.412183	42.326367	Guara	Lutetian
137	-0.411233	42.329683	Guara	Lutetian
138	-0.428667	42.305850	Guara	Lutetian
139	-0.448000	42.303667	Guara	Lutetian
141	-0.446800	42.294267	Guara	Lutetian
142	-0.442767	42.310567	Guara	Lutetian
144	-0.393750	42.345333	Guara	Lutetian
145	-0.418917	42.324983	Guara	Lutetian
146	-0.402833	42.335867	Guara	Lutetian
444	-0.412102	42.325097	Guara	Lutetian
445	-0.412098	42.325157	Guara	Lutetian
467	-0.405834	42.312462	Guara	Lutetian
469	-0.405920	42.312555	Guara	Lutetian
470	-0.405842	42.312665	Guara	Lutetian
472	-0.405998	42.312688	Guara	Lutetian
473	-0.406108	42.312823	Guara	Lutetian
474	-0.406552	42.313484	Guara	Lutetian
475	-0.406526	42.313602	Guara	Lutetian
497	-0.419564	42.306512	Guara	Lutetian
498	-0.420014	42.306393	Guara	Lutetian
499	-0.420358	42.306254	Guara	Lutetian
500	-0.429013	42.304032	Guara	Lutetian
503	-0.403275	42.306514	Guara	Lutetian
515	-0.416279	42.323905	Guara	Lutetian
519	-0.414092	42.322768	Guara	Lutetian
520	-0.412027	42.319628	Guara	Lutetian
493	-0.411017	42.309405	Adrean-Bona	Cretaceous
489	-0.407789	42.310467	Tremp	Cretaceous
490	-0.407872	42.310662	Tremp	Cretaceous
553	-0.401047	42.285117	Triassic	Triassic
555	-0.401272	42.286006	Triassic	Triassic

Site number in italic: site where samples for isotopic analysis were taken